JPn Neuroscience

The Journal of Physiology

*J Physiol* 00.00 (2013) pp 1–23



# Selective mitochondrial $Ca^{2+}$ uptake deficit in disease endstage vulnerable motoneurons of the $SOD1^{G93A}$ mouse model of amyotrophic lateral sclerosis

Andrea Fuchs[1,4], Sylvie Kutterer[1], Tobias Mühling[2], Johanna Duda[2], Burkhard Schütz[3], Birgit Liss[2], Bernhard U. Keller[4] and Jochen Roeper[1]

[1]*Institute for Neurophysiology, Goethe-University Frankfurt, Theodor-Stern-Kai 7, 60590 Frankfurt, Germany*
[2]*Institute of Applied Physiology, University of Ulm, Albert-Einsteinallee 11, 89081 Ulm, Germany*
[3]*Institute of Anatomy and Cell Biology, Philipps-University Marburg, Robert-Koch-Straße 8, 35037 Marburg, Germany*
[4]*Center of Physiology, Georg-August-University Göttingen, Humboldtallee 23, 37073 Göttingen, Germany*

**Key points**

- So far, increased excitability and calcium handling problems have been discussed as causes for motoneuron death in amyotrophic lateral sclerosis (ALS) mainly on the basis of studies in juvenile presymptomatic mice.
- We developed a brainstem preparation to analyse excitability and calcium handling during disease progression up to disease endstage of motoneurons in an ALS mouse model.
- Increased excitability of motoneurons is not seen at disease endstage, challenging this factor as a direct cause for motoneuron death in ALS.
- We show that calcium handling is remodelled during disease progression from mitochondrial uptake to mitochondrial uptake failure and increased plasma membrane extrusion, providing a compensatory mechanism that fails at disease endstage and might lead to a toxic calcium overload of the cells.
- Supporting this newly described compensatory endeavour of the motoneurons might be a promising therapeutic strategy.

**Abstract** Amyotrophic lateral sclerosis is a progressive neurodegenerative disease that targets some somatic motoneuron populations, while others, e.g. those of the oculomotor system, are spared. The pathophysiological basis of this pattern of differential vulnerability, which is preserved in a transgenic mouse model of amyotrophic lateral sclerosis ($SOD1^{G93A}$), and the mechanism of neurodegeneration in general are unknown. Hyperexcitability and calcium dysregulation have been proposed by others on the basis of data from juvenile mice that are, however, asymptomatic. No studies have been done with symptomatic mice following disease progression to the disease endstage. Here, we developed a new brainstem slice preparation for whole-cell patch-clamp recordings and single cell fura-2 calcium imaging to study motoneurons in adult wild-type and $SOD1^{G93A}$ mice up to disease endstage. We analysed disease-stage-dependent electrophysiological properties and intracellular $Ca^{2+}$ handling of vulnerable hypoglossal motoneurons in comparison to resistant oculomotor neurons. Thereby, we identified a transient hyperexcitability in presymptomatic but not in endstage vulnerable motoneurons. Additionally, we revealed a remodelling of intracellular $Ca^{2+}$ clearance within vulnerable but not resistant motoneurons at disease endstage characterised by a reduction of uniporter-dependent mitochondrial $Ca^{2+}$ uptake and enhanced $Ca^{2+}$ extrusion across the plasma membrane. Our study challenged the notion that hyperexcitability is a direct cause

B. U. Keller and J. Roeper are equal senior authors.



DOI: 10.1113/jphysiol.2012.247981

of neurodegeneration in SOD1$^{G93A}$ mice, but molecularly identified a $Ca^{2+}$ clearance deficit in motoneurons and an adaptive $Ca^{2+}$ handling strategy that might be targeted by future therapeutic strategies.

(Received 12 November 2012; accepted after revision 4 February 2013; first published online 11 February 2013)
**Corresponding author** A. Fuchs: Mammalian Locomotor Laboratory, Department of Neuroscience, Karolinska Institutet, Retzius Väg 8, 17177 Stockholm, Sweden. Email: andrea.fuchs@ki.se

**Abbreviations** ALS, amyotrophic lateral sclerosis; AP, action potential; cAHP, compound afterhyperpolarisation; ChAT, choline-acetyl transferase; ER, endoplasmic reticulum; HMN, hypoglossal motoneuron; mCU, mitochondrial calcium uniporter; MCU, mitochondrial calcium uniporter (molecular component of mCU); MICU1, mitochondrial calcium uptake 1 (molecular component of mCU); MN, motoneuron; mNCX, mitochondrial $Na^+/Ca^{2+}$ exchanger; NCX, $Na^+/Ca^{2+}$ exchanger; OMN, oculomotor motoneuron; P, postnatal day; PIC, persistent inward current; PMCA, plasma membrane $Ca^{2+}$ ATPase; RT-qPCR, real-time quantitative polymerase chain reaction; SOD1, superoxide dismutase 1; UV-LMD, UV laser microdissection; WT, wild-type.

## Introduction

Amyotrophic lateral sclerosis (ALS) is a rare adult-onset neurodegenerative disease, which is characterised by the preferential loss of cortical, brainstem and spinal motoneurons (MNs) (Kiernan *et al.* 2011). As there is currently no effective treatment, death occurs in ALS patients usually 3–5 years after initial diagnosis. In about 10% of the cases, ALS is caused by hereditary mutations (familial ALS) in a number of identified disease genes, very prominently among them gain-of-function mutations in the superoxide dismutase 1 (SOD1) gene (Ticozzi *et al.* 2011). The aetiology of the majority of sporadically occurring ALS cases remains unknown. The similar phenotype of MN degeneration of sporadic and familial ALS suggests related molecular events acting within vulnerable target neurons at final disease stages. There is evidence that general disease processes like glutamate excitotoxicity, $Ca^{2+}$ overload and oxidative stress as proposed for many other neurological disorders are also implicated in MN death in ALS. In addition to synaptic overexcitation, an intrinsic hyperexcitability of MNs associated with increased persistent inward currents (PICs) was described in human patients as well as in juvenile presymptomatic stages of ALS mouse models (Pieri *et al.* 2003; Kuo *et al.* 2004, 2005; Kanai *et al.* 2006; Amendola *et al.* 2007; Bories *et al.* 2007; van Zundert *et al.* 2008; Pambo-Pambo *et al.* 2009; Vucic & Kiernan, 2010; Quinlan *et al.* 2011).

MNs are believed to be preferentially vulnerable to overexcitation as they possess $Ca^{2+}$-permeable AMPA receptors and low $Ca^{2+}$ buffering capacity (Alexianu *et al.* 1994; Carriedo *et al.* 1996; Lewinski & Keller, 2005; Gou-Fabregas *et al.* 2009). The reduced buffering capacity is due to low expression levels of $Ca^{2+}$ buffering proteins like parvalbumin or calbindin-D28K in vulnerable MNs but not in resistant oculomotor neurons (Alexianu *et al.* 1994; Vanselow & Keller, 2000; Lewinski *et al.* 2008). This might contribute to the differential vulnerability of distinct MN populations in ALS (Nimchinsky *et al.*2000; Haenggeli & Kato, 2002; Lewinski & Keller, 2005). Compared to the minor contribution of $Ca^{2+}$ buffering proteins, mitochondrial $Ca^{2+}$ uptake has a large impact in vulnerable MNs (Jaiswal & Keller, 2009). It was previously described that mitochondrial shape and function are disturbed in ALS. Functional deficits concerning $Ca^{2+}$ uptake and handling were also detectable. Several studies showed a not further analysed reduced mitochondrial $Ca^{2+}$ uptake capacity in isolated mitochondria, MNs or motor terminals of ALS models (Kruman *et al.* 1999; Vila *et al.* 2003; Damiano *et al.* 2006; Jaiswal & Keller, 2009; Coussee *et al.* 2011). The mitochondrial membrane potential, the driving force for $Ca^{2+}$ uptake, was found to be depolarised or $Ca^{2+}$-induced depolarisation was increased (Carrì *et al.* 1997; Damiano *et al.* 2006; Jaiswal & Keller, 2009; Nguyen *et al.* 2009). Taken together, these effects might lead to higher intracellular $Ca^{2+}$ levels (Carrì *et al.* 1997; Kruman *et al.* 1999) and thus contribute to MN death in ALS.

Similar to most $Ca^{2+}$ imaging studies, electrophysiological descriptions of disease-related MN changes in ALS animal models have mainly focused on cell culture or mice younger than postnatal day 12 (P12). The observed changes were linked to developmental irregularities but were also discussed as potential causes for the degenerative process itself (Amendola *et al.* 2007; Lewinski *et al.* 2008; Quinlan *et al.* 2011). However, the most common ALS mouse model, a transgenic mouse (SOD1$^{G93A}$) expressing a disease-causing variant (G93A) of the human superoxide dismutase 1 (SOD1) gene in high copy number (Gurney *et al.* 1994), does not display any MN loss at this juvenile age (Chiu *et al.* 1995), but shows adult disease onset (first tongue motor deficits at P77; Fuchs *et al.* 2010). Only at an age of >69 days, do SOD1$^{G93A}$ mice show significant loss of vulnerable spinal MNs (Chiu *et al.* 1995) (>10% at P80), with an increase to about 70% cell loss at the time of death around P130 (Schütz, 2005). Therefore, it will be difficult to draw direct links to MN degeneration from investigations limited to embryonic or early postnatal stages.

Here, we introduce a preparation of adult brainstem slices that allowed us to study MN characteristics throughout the entire disease progression up to the final stage (disease endstage). We used patch-clamp electrophysiology, fluorometric methods and quantitative gene expression analyses to reveal general properties and disease-related changes of excitability and $Ca^{2+}$ handling in age-matched adult wild-type (WT) and endstage $SOD1^{G93A}$ ALS mouse MNs. We focused on the vulnerable brainstem MNs of the hypoglossal nucleus (HMNs) and compared them with adult presymptomatic (P70) HMNs as well as resistant oculomotor neurons (OMNs) to identify those mechanisms that are both disease-stage specific and relevant in the context of differential vulnerability.

## Methods

### Ethical approval

All animal procedures were approved by Regierungspräsidium Darmstadt and Tübingen (Germany) and conducted according to the guidelines of the German Tierschutzgesetz.

### Brain slice preparation

For all experiments male transgenic mice of the strain B6SJL-TgN(SOD1-G93A)1Gur (Jackson Laboratory, Bar Harbor, ME, USA) and their WT littermates were used. Mice were bred on site and genotyped according to the protocol recommended by Jackson Laboratory. $SOD1^{G93A}$ mice aged postnatal day P70 ± 5 (referred to as P70) were classified as late presymptomatic according to tongue movement ability (Fuchs *et al.* 2010). For endstage analyses, $SOD1^{G93A}$ mice between P115 and P140 (referred to as P120 or endstage) were used after they were no longer able to pass a paw grip endurance test (clinical score 4; Solomon *et al.* 2011) and results were compared to age-matched WT littermates.

Mice were deeply anaesthetised with an ip injection of 250 mg/kg ketamine (Inresa, Freiburg, Germany) and 2.5 mg/kg medetomidine hydrochloride (Pfizer, Berlin, Germany) and intracardially perfused with ice-cold artificial cerebrospinal fluid (50 ml/min for 3 min; perfusion ACSF: in mM: 125 NaCl, 2.5 KCl, 25 $NaHCO_3$, 1.25 $NaH_2PO_4$, 2.5 glucose, 50 sucrose, 0.1 $CaCl_2$, 6 $MgCl_2$, 3 kynurenic acid, oxygenated with 95% $O_2$, 5% $CO_2$). Perfused mice were decapitated with preservation of the first 1–2 cervical vertebral bodies. With fine scissors these remaining vertebral bodies were cut dorsally, thus entering the foramen magnum and following the sagittal suture of the skull until bregma. Bones were folded aside. The brain was cut coronally with a razor blade at bregma and the caudal part was quickly removed from the skull avoiding a pull on the basal nerves by proper sectioning with fine scissors. Brains were glued on a specimen holder and coronal slices (250 $\mu$m) containing the hypoglossal (bregma −8 to −5 mm) or the oculomotor nucleus (bregma −5 to −3 mm) were cut by a vibratome with minimised vertical deflection (VT1200S, Leica, Wetzlar, Germany) in the ice-cold perfusion ACSF. Slices recovered for 90 min at 36°C in bubbled recording ACSF (in mM: 125 NaCl, 2.5 KCl, 25 $NaHCO_3$, 1.25 $NaH_2PO_4$, 2.5 glucose, 22.5 sucrose, 2 $CaCl_2$, 2 $MgCl_2$, oxygenated with 95% $O_2$, 5% $CO_2$) and stored at room temperature until transfer to patch-clamp bath chamber (up to 6 h).

### Patch-clamp analysis

Slices were superfused with oxygenated recording ACSF. CNQX, 10 $\mu$M, and SR95531, 4 $\mu$M (both Biotrend, Cologne, Germany), were added to block fast excitatory and inhibitory inputs, respectively. All experiments were performed at 36°C. Patch pipettes (3.5–4.5 MΩ) were pulled from borosilicate glass (GC150TF-10, Harvard Apparatus, Holliston, MA, USA) and filled with (in mM): 135 potassium gluconate, 5 KCl, 10 Hepes, 0.1 EGTA, 2 $MgCl_2$, pH 7.35 for the basal electrophysiological characterisation of P70 and endstage HMNs. Neurons were visualised by video microscopy (Axioskop 2 FS plus, Zeiss, Göttingen, Germany) using transversal illumination for increasing contrast. Whole-cell patch-clamp recordings were performed using an EPC-10 amplifier (Heka Electronics, Lambrecht, Germany). Data were sampled with 20 kHz and low-pass filtered with 5 kHz. Voltage-clamp data were further digitally filtered with 100 Hz. Only recordings with uncompensated series resistance under 15 MΩ were analysed. Results were not corrected for liquid junction potential, which is estimated to be less than 5 mV.

### Fluorometric measurements

For all imaging experiments and $Ca^{2+}$-dependent electrophysiological data of Fig. 3, the pipette solution was modified as follows (in mM): 135 potassium gluconate, 5 KCl, 10 Hepes, 2 $MgCl_2$, 0.2 fura-2, 2 Na-ATP, 0.2 Li-GTP, pH 7.35. To avoid cell depolarisation by extracellularly puffed ATP we added 0.1 mM pyridoxalphosphate-azophenyl-disulfonate (PPADS, Biotrend) to the ACSF to block P2X receptors. Fura-2 (Invitrogen, Eugene, OR, USA) and Rhodamine 123 (Rh-123, Invitrogen) fluorescence was visualised using a CCD camera system (TILL Photonics, Graefelfing, Germany): a computer-controlled monochromator was connected to the microscope via fibre optics (objective Achroplan 40×, W, Ph 2, NA 0.8). Fluorescence was detected by a 12-bit CCD camera (IMAGO QE, TILL

Photonics). Binning was set to $4 \times 4$ and sampling frequency was either 2 Hz for $Ca^{2+}$ imaging or 1 Hz for Rh-123 recordings. Data were recorded in a region of interest drawn over the cell soma using LiveAcquisition software (TILL Photonics).

For mitochondrial membrane potential estimation slices were incubated at room temperature in 0.25 $\mu$g ml$^{-1}$ Rh-123 for 10 min and washed in the recording chamber at 36°C for >30 min. Rh-123 accumulates in mitochondria and its fluorescence is quenched. Rh-123 was released by mitochondrial uncoupling with 5 $\mu$M carbonyl cyanide 4-trifluomethoxy-phenylhydrazone (FCCP, Tocris, Bristol, UK) and excited with 485 nm. Data were plotted as relative fluorescence values $F/F_0$ with $F$ denoting the fluorescence at different time points and $F_0$ the baseline fluorescence before uncoupling.

Somatic $Ca^{2+}$ concentration changes were imaged after loading the cells with fura-2 for >10 min via the patch pipette. The fura-2 dissociation constant ($K_d$) was determined by performing an *in vitro* calibration according to the Invitrogen protocol (Molecular Probes, Calcium Calibration Buffer Kit, 2011) and estimated as $K_d = 154$ nM. Fura-2 was excited alternately at 357 nm and 380 nm to gain ratiometric $Ca^{2+}$ measurements. Data were plotted as $F/F_0$ with $F$ denoting the fluorescence ratio at different time points and $F_0$ the ratio at the beginning of the recordings. For pharmacological modification, Ruthenium 360 (Ru360, 20 $\mu$M, Calbiochem, Darmstadt, Germany) or CPG37157 (15 $\mu$M, Biotrend) were added to the pipette solution, FCCP (200 nM or 80 nM for HMNs or OMNs, respectively) and thapsigargin (1 $\mu$M, Biotrend) were applied via the bath perfusion system.

## Data acquisition and analysis

Electrophysiological characterisation was performed in whole-cell current-clamp configuration by applying positive (holding potential −60 mV) or negative (from resting potential) current steps and ramps. Action potential characteristics were analysed as the mean of three steady-state action potentials (APs) at a firing frequency of 40 Hz. The compound after-hyperpolarisation (cAHP) amplitude was assessed after 40 Hz firing. PIC characteristics were recorded in voltage-clamp mode by applying a slow voltage ramp (18 mV s$^{-1}$) from −70 mV to −20 mV. Currents were leak corrected. Currents in the presence of 300 nM tetrodotoxin (TTX) were subtracted from control recordings to gain TTX-sensitive currents.

For $Ca^{2+}$ imaging, somatic $Ca^{2+}$ influx was evoked by increasing current steps of 2 s duration. The next step was applied after complete recovery of the $Ca^{2+}$ signal. Fluorescence decay was fitted by a mono-exponential function whenever possible and decay time constant ($\tau$) was calculated. The area under the curve of the $Ca^{2+}$ signal starting from 90% of the maximal amplitude was analysed and normalised to the signal amplitude. Arbitrary units (AU), defined as the normalised area divided by 1000, are plotted. $\tau$ and signal area were correlated to the firing frequency. For statistics, the signals evoked by a firing frequency of 40 Hz and by maximal firing frequency ($f_{max}$) were compared. For pharmacological experiments with bath application of the blocker, only one cell per slice was recorded.

Electrophysiological and imaging data were analysed and plotted using IgorPro (WaveMetrics, Lake Oswego, OR, USA) with custom or NeuroMatic (Think Random, London, UK) routines and Prism5 (GraphPad Software, La Jolla, CA, USA). Statistics were performed with Prism5. Data are shown as scatter plots with mean or as histograms with mean ± standard error of the mean (SEM). Cell number is abbreviated with $n$, animal number with $N$. Values were tested for normal distribution with the D'Agostino–Pearson test. For statistical comparison of two groups, Student's $t$ tests were carried out if the values were normally distributed. The Mann–Whitney $U$ test was used if the values were not normally distributed. Statistical significance was set at $P < 0.05$ (*), $P < 0.01$ (**) or $P < 0.001$ (***).

## Immunohistochemistry

For confirmation of the MN identity cells were filled with 1 mg ml$^{-1}$ neurobiotin (Vector Laboratories, Peterborough, UK) during whole-cell recordings. Slices were fixed in 4% paraformaldehyde and 15% picric acid in PBS, pH 7.4 over night and stained with a choline acetyltransferase (ChAT) antibody (1:250, AB144P, Chemicon, Temecula, CA, USA). Slices were incubated in Alexa Fluor 568 streptavidin (1:750, Molecular Probes, Eugene, OR, USA) for the detection of neurobiotin and Alexa Fluor 488 anti-goat IgG (1:1000, Molecular Probes) for the detection of ChAT. Double labelling was determined using a confocal laser-scanning microscope (LSM 510, Zeiss, Göttingen, Germany).

## UV laser microdissection and quantitative real-time PCR

Tissue sectioning, UV laser microdissection (UV-LMD), reverse transcription as well as qualitative multiplex nested PCR and quantitative real-time PCR (RT-qPCR) were performed as previously described (Grundemann *et al.* 2008). For details see Supplemental Methods and Supplemental Table S1 (available online only). To control the specificity of harvested HMN pools, ~1/3 of cDNA (5 $\mu$l) was utilised for qualitative multiplex-nested PCR of the selected marker genes choline

acetyltransferase (*ChAT*), glial fibrillary acidic protein (*GFAP*) and glutamate decarboxylase (*GAD65/67*). Only ChAT-positive and GAD65/67-negative HMN pools were further analysed (Fig. 9*A* and *B*). Quantitative PCR was carried out using TaqMan assays utilising a GeneAmp 7900HT (Applied Biosystems, Darmstadt, Germany). Data analysis was performed with SDS2.3 software (Applied Biosystems). Relative expression data are given as mean ± SEM, normalised to WT and as MCU/MICU1 ratio. For statistical comparison, Mann-Whitney-U tests were carried out.

## Results

### Adult presymptomatic $SOD1^{G93A}$ hypoglossal motoneurons show hyperexcitability that is absent when they reach disease endstage

We developed an acute slice preparation to perform whole-cell patch-clamp recordings of adult hypoglossal motoneurons (HMNs; Fig. 1*A*) and oculomotor neurons (OMNs) of $SOD1^{G93A}$ and littermate wild-type (WT) control mice. Here we report data from mice ranging from an adult but still presymptomatic stage (∼P70) up to disease endstage (∼P120), when animals are severely motor-impaired. HMNs localised in the more vulnerable ventral part of the nucleus were identified during visually guided patch-clamp experiments by established functional properties and cell size (capacitance >30 pF). In addition, the MN identity and location of some HMNs and all OMNs were verified by neurobiotin filling and choline acetyltransferase (ChAT) double immunostaining (Fig. 1*B* and *C*).

To characterise electrophysiological properties of adult brainstem MNs and to reveal possible disease-related changes, we compared the basal electrophysiological properties of HMNs in WT and $SOD1^{G93A}$ mice for the adult presymptomatic stage as well as disease endstage (for values and the complete set of electrophysiological data see Table 1). WT and $SOD1^{G93A}$ MNs differed only in a few parameters, i.e. the resting membrane potential was slightly but significantly more hyperpolarised in endstage $SOD1^{G93A}$ compared to age-matched WT HMNs. Action potential (AP) thresholds were significantly more hyperpolarised in adult presymptomatic and significantly more depolarised in endstage $SOD1^{G93A}$ neurons compared to WT controls (Fig. 1*D*). All cells responded to positive current steps with similar regular firing (Fig. 1*E*) and displayed a similar prominent sag upon hyperpolarisation (Fig. 1*F*), indicative of the presence of a hyperpolarisation activated current ($I_h$).

The slope of the frequency–current relationship (*f–I*) as a measure of excitability was significantly larger in adult P70 presymptomatic $SOD1^{G93A}$ HMNs compared to age-matched WT controls (Fig. 2*A*), in line with previous studies on juvenile mice (<P10, van Zundert *et al.* 2008) indicating hyperexcitability. In contrast, the *f–I* slopes of WT and endstage $SOD1^{G93A}$ HMNs were not different (Fig. 2*B*), indicating the absence of intrinsic hyperexcitability in endstage $SOD1^{G93A}$ vulnerable MNs.

Persistent inward currents (PICs) are proposed to underlie the hyperexcitability of motoneurons in ALS models (Kuo *et al.* 2005). Figure 2*C* and *D* shows representative TTX-sensitive PICs recorded in WT, adult presymptomatic and endstage $SOD1^{G93A}$ HMNs, respectively. In contrast to earlier studies, both absolute inward current (data not shown) and current density were similar for WT and $SOD1^{G93A}$ in both age groups (for values see Table 2). In addition, we found no differences in the voltage-dependence of PIC conductances ($V_{50}$; Fig. 2*C* and *D* right panel). Current ramp protocols revealed only a small trend towards a clockwise hysteresis (i.e. for any current, the firing frequency is little higher during the ascending ramp than the descending) in both genotypes, being more prominent in P70 mice (Supplemental Fig. S1) indicative of a low and, during disease progression, decreasing impact of PICs (Hounsgaard *et al.* 1988). Significantly less current was necessary to evoke APs in presymptomatic $SOD1^{G93A}$ HMNs compared to WT on the ascending ramp (Table 1). Taken together, our results for the first time described electrophysiological characteristics of adult HMNs and revealed a transient hyperexcitability in adult presymptomatic $SOD1^{G93A}$ HMNs compared to age-matched WT controls, which is absent at disease endstage in line with no differences in PIC characteristics.

### The compound afterhyperpolarisation is selectively increased in vulnerable endstage MNs

Given the absence of hyperexcitability *per se* in vulnerable MNs during disease endstage, we focused on excitability-related changes in $Ca^{2+}$ handling as a second proposed degeneration-related factor. Here, we observed a selective increase of the compound afterhyperpolarisation (cAHP) amplitude induced by a 40 Hz train of action potentials in endstage $SOD1^{G93A}$ HMNs compared to age-matched WT controls (Fig. 3*B*, Table 1). However, no genotype-associated difference was observed for cAHPs in presymptomatic HMNs (Fig. 3*A*, Table 1) or endstage OMNs (WT: 4.90 ± 0.60 mV, $n = 25$, $N = 6$; $SOD1^{G93A}$: 5.91 ± 0.41 mV, $n = 26$, $N = 4$; Fig. 3*C*). In contrast to the differences in cAHP amplitudes, the decay kinetics of the cAHPs were not different in endstage, but slower in presymptomatic $SOD1^{G93A}$ HMNs compared to WT (Table 1). Since the cAHP is mainly driven by $Ca^{2+}$-activated potassium channels (amplitude reduction by paxilline and apamin, data not shown), the results suggested a larger

activity-dependent increase of cytosolic $Ca^{2+}$ selectively in endstage SOD1$^{G93A}$ HMNs. Consequently, we focused on a direct assessment of activity-dependent $Ca^{2+}$ handling in these neurons using imaging techniques.

## An activity-dependent $Ca^{2+}$ clearance deficit is selective for vulnerable endstage MNs

To directly study the $Ca^{2+}$ handling properties of MNs, we used single-cell fura-2 $Ca^{2+}$ imaging in combination

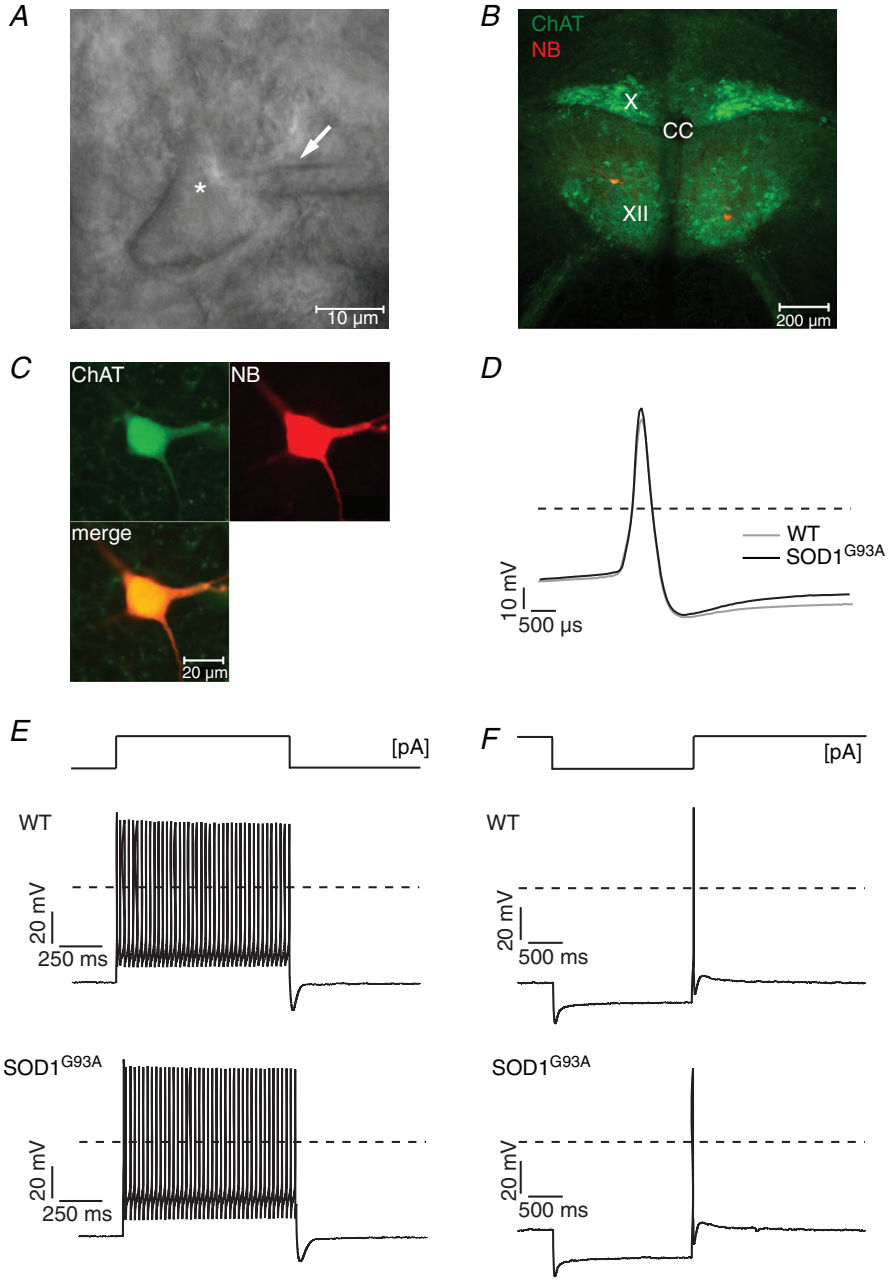


**Figure 1. Electrophysiological characterisation of adult HMNs in WT and endstage SOD1$^{G93A}$ mice**
*A*, hypoglossal motoneuron (HMN) in a P116 SOD1$^{G93A}$ mouse (*). Arrow indicates the patch pipette. *B* and *C*, confocal image of the hypoglossal nucleus with two recorded and filled cells (*B*) and a HMN in higher magnification (*C*). XII: hypoglossal nucleus. X: dorsal nucleus of the vagus. CC: central canal. MN identity was verified by neurobiotin filling (NB, red) and choline acetyltransferase double labelling (ChAT, green). *D*, action potentials of a representative WT and an endstage SOD1$^{G93A}$ HMN. Note the slightly but significantly depolarised threshold in SOD1$^{G93A}$ and the short duration of adult MN APs. *E*, depolarising current steps evoked repetitive firing in whole-cell current-clamp mode similar for a representative WT and endstage SOD1$^{G93A}$ HMN. *F*, negative current steps evoked hyperpolarisation similar for a representative WT and endstage SOD1$^{G93A}$ HMN. Note the sag component and the rebound spike. Dashed lines at 0 mV. For mean values of all parameters see Table 1.

**Table 1. Electrophysiological properties of adult HMNs in WT, presymptomatic and endstage $SOD1^{G93A}$**

| HMN P70 | | | |
|---|---|---|---|
| | WT ($N = 6$/#6) | $SOD1^{G93A}$ ($N = 7$/#3) | *P* value |
| Capacitance (pF) | 64.95 ± 2.17, $n = 76$ | 60.19 ± 1.48, $n = 102$ | 0.14 |
| $R_i$ (MΩ) | 110.37 ± 5.26, $n = 74$ | 123.38 ± 5.37, $n = 99$ | 0.17 |
| RMP (mV) | −45.26 ± 0.46, $n = 76$ | −45.91 ± 0.41, $n = 102$ | 0.11 |
| Rheobase (pA) | 259.05 ± 16.43, $n = 76$ | 202.81 ± 10.88, $n = 102$ | 0.009** |
| $I_{off}$ (pA) | 308.86 ± 18.28, $n = 76$ | 236.13 ± 12.14, $n = 102$ | 0.003** |
| AP threshold (mV) | −33.56 ± 0.39, $n = 76$ | −34.98 ± 0.31, $n = 102$ | 0.004** |
| AP amplitude (mV) | 98.53 ± 0.57, $n = 76$ | 97.26 ± 0.64, $n = 102$ | 0.17 |
| AP duration ($\mu$s) | 1105.68 ± 26.00, $n = 76$ | 1036.57 ± 17.65, $n = 102$ | 0.06 |
| fAHP amplitude (mV) | 23.06 ± 0.42, $n = 76$ | 23.61 ± 0.36, $n = 102$ | 0.32 |
| cAHP amplitude (mV) | 8.16 ± 0.49, $n = 28$# | 9.37 ± 0.46, $n = 28$# | 0.27 |
| cAHP $\tau$ (ms) | 97.02 ± 6.28, $n = 33$# | 80.79 ± 6.19, $n = 26$# | 0.007** |
| $f_{max}$ (Hz) | 130.43 ± 3.50, $n = 76$ | 136.27 ± 4.32, $n = 102$ | 0.54 |
| *f–I* slope (Hz $pA^{-1}$) | 0.099 ± 0.008, $n = 76$ | 0.125 ± 0.007, $n = 99$ | 0.0001*** |
| Sag (mV) | 13.24 ± 0.49, $n = 74$ | 13.33 ± 0.26, $n = 99$ | 0.52 |
| **HMN P120** | | | |
| | WT ($N = 26$/#7) | $SOD1^{G93A}$ ($N = 26$/#5) | *P* value |
| Capacitance (pF) | 54.37 ± 1.69, $n = 78$ | 53.35 ± 1.34, $n = 96$ | 0.92 |
| $R_i$ (MΩ) | 100.50 ± 5.74, $n = 51$ | 105.60 ± 4.17, $n = 84$ | 0.3 |
| RMP (mV) | −49.52 ± 0.43, $n = 64$ | −51.10 ± 0.35, $n = 84$ | 0.005** |
| Rheobase (pA) | 242.20 ± 19.97, $n = 34$ | 217.40 ± 20.29, $n = 36$ | 0.39 |
| $I_{off}$ (pA) | 304.70 ± 22.14, $n = 34$ | 244.40 ± 20.34, $n = 36$ | 0.049* |
| AP threshold (mV) | −30.40 ± 0.53, $n = 78$ | −28.72 ± 0.57, $n = 96$ | 0.048* |
| AP amplitude (mV) | 71.15 ± 0.92, $n = 78$ | 70.87 ± 0.91, $n = 96$ | 0.83 |
| AP duration ($\mu$s) | 893.80 ± 22.14, $n = 78$ | 922.10 ± 19.88, $n = 96$ | 0.46 |
| fAHP amplitude (mV) | 19.70 ± 0.43, $n = 78$ | 18.54 ± 0.48, $n = 96$ | 0.22 |
| cAHP amplitude (mV) | 6.55 ± 0.51, $n = 24$# | 9.71 ± 0.62, $n = 26$# | 0.0003*** |
| cAHP $\tau$ (ms) | 102.90 ± 13.79, $n = 24$# | 88.10 ± 12.67, $n = 26$# | 0.42 |
| $f_{max}$ (Hz) | 145.80 ± 5.40, $n = 78$ | 145.00 ± 5.20, $n = 96$ | 0.68 |
| *f–I* slope (Hz $pA^{-1}$) | 0.075 ± 0.004, $n = 78$ | 0.071 ± 0.004, $n = 96$ | 0.57 |
| Sag (mV) | 11.62 ± 0.46, $n = 48$ | 11.39 ± 0.34, $n = 77$ | 0.69 |

Statistical significance as indicated. #, values from electrophysiological recordings during $Ca^{2+}$ imaging with modified protocol and solutions. AP, action potential; cAHP, compound afterhyperpolarisation in response to a 2 s train of action potentials at 40 Hz; fAHP, fast afterhyperpolarisation after single action potential; *f–I* slope, slope of frequency–current curve; $f_{max}$, maximal firing frequency; $I_{off}$, current on descending ramp at cessation of firing; $R_i$, input resistance; RMP, resting membrane potential; $\tau$, time constant.

with standard whole-cell patch-clamp recordings in MNs from presymptomatic adult and disease end-stage mice. Figure 4*A* shows an example of a HMN filled with fura-2 via the patch pipette. We recorded changes of fluorescence intensities over the cell soma and applied increasing current steps to drive action potential discharges up to maximal sustained firing frequencies before depolarisation block (Fig. 4*B*). Ratiometric fura-2 signals increased in amplitude with increasing firing frequencies and returned to baseline level at the end of stimulation with a time course that was well described by a mono-exponential function (see fits with time constant ($\tau$, arrows) in red in Fig. 4*C–E*), both after 40 Hz or maximal frequency discharge in WT (Fig. 4*C–E*, left panels) or $SOD1^{G93A}$ MNs (Fig. 4*C–E*, middle panels). The right panels of Fig. 4*C* and *D* depict the frequency dependencies of $\tau$ and of the fluorescence signal area normalised to signal peak for representative adult presymptomatic and endstage $SOD1^{G93A}$ HMNs and WT controls. Figure 4*E* shows activity-dependent $Ca^{2+}$ signalling for the resistant endstage $SOD1^{G93A}$ and WT OMNs.

Although the maximal firing frequencies were distinct for individual MN populations and ages ranging from 90 to 300 Hz in HMNs and from 200 to 380 Hz in OMNs (during the calcium imaging experiments), they were not significantly different between age-matched WT and $SOD1^{G93A}$ cells (P70 HMNs: WT: 174.69 ± 12.11 Hz, $n = 35$, $N = 6$; $SOD1^{G93A}$: 200.69 ± 10.90 Hz, $n = 26$, $N = 3$; $P = 0.17$; endstage HMNs: WT: 201.60 ± 14.19 Hz, $n = 23$, $N = 7$; $SOD1^{G93A}$: 198.30 ± 11.23 Hz, $n = 26$,

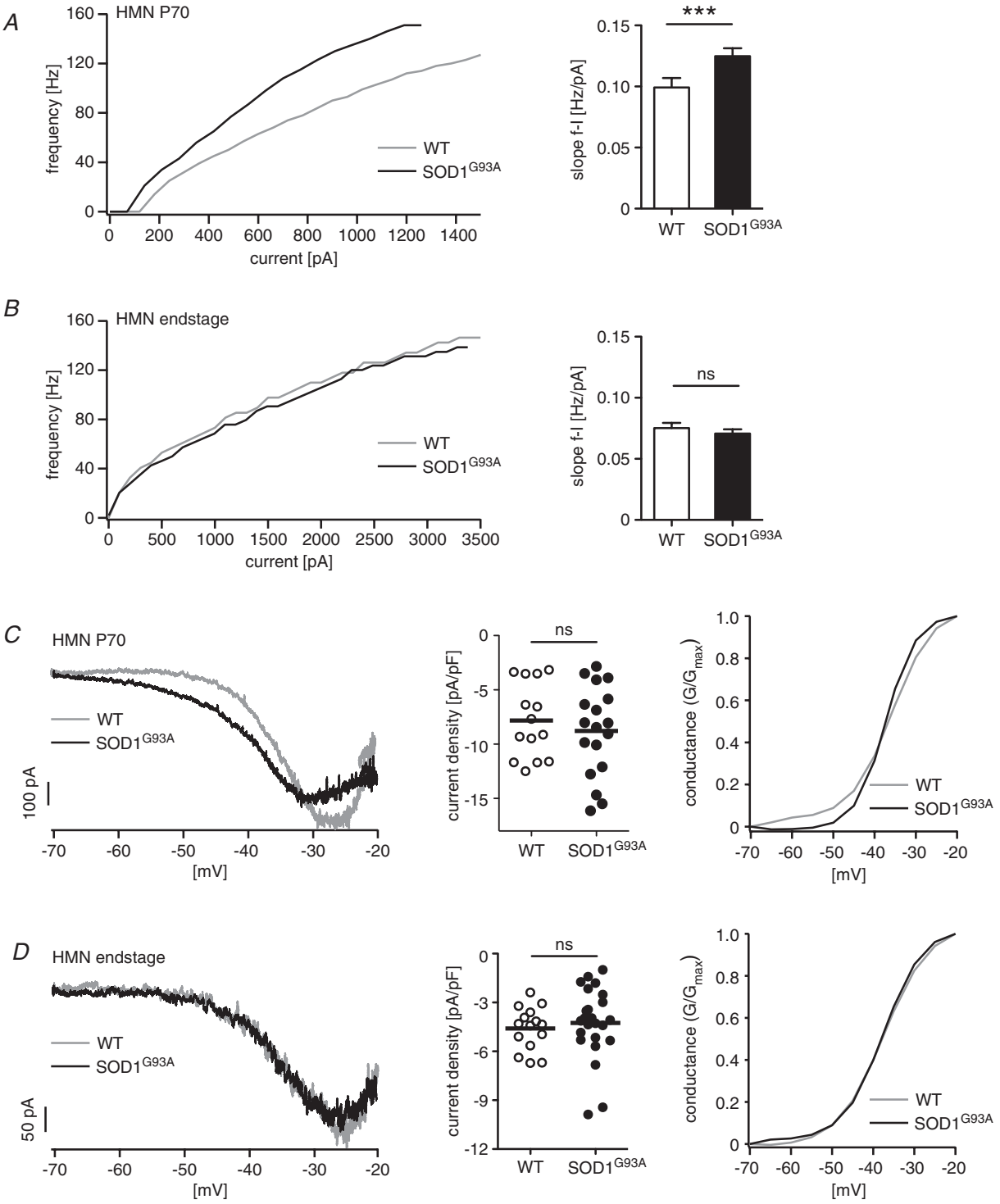


**Figure 2. Hyperexcitability is apparent in presymptomatic but not disease endstage SOD1$^{G93A}$ HMNs**
*A* and *B*, representative frequency–current plot (*f–I*, left panel) and mean *f–I* slopes (right panel) of presymptomatic SOD1$^{G93A}$ and age-matched WT HMNs (*A*) and endstage SOD1$^{G93A}$ and age-matched WT HMNs (*B*). Statistical significance as indicated. For values see Table 1. Note the steeper *f–I* curves indicative for hyperexcitability only in presymptomatic not in endstage SOD1$^{G93A}$ MNs compared to controls. *C* and *D*, representative TTX-sensitive persistent inward currents (left panel), single cell values and mean current densities (middle panel) and mean sigmoidal fits of conductance–voltage relationships (right panel) of presymptomatic SOD1$^{G93A}$ and age-matched WT HMNs (*C*) or endstage SOD1$^{G93A}$ and age-matched WT HMNs (*D*). Currents were evoked by voltage ramps; currents after TTX application were subtracted from currents before TTX application. Note that PIC parameters are similar in WT and age-matched SOD1$^{G93A}$ HMNs. ns, not significant. For values see Table 2.

**Table 2. Properties of persistent inward currents in adult HMNs in WT, presymptomatic and endstage $SOD1^{G93A}$**

| | HMN P70 | | |
|---|---|---|---|
| | WT ($n = 14$, $N = 6$) | $SOD1^{G93A}$ ($n = 18$, $N = 4$) | *P* value |
| PIC absolute (pA) | −499.73 ± 75.66 | −447.19 ± 72.14 | 0.62 |
| PIC density (pA $pF^{-1}$) | −8.53 ± 0.92 | −8.78 ± 0.98 | 0.86 |
| PIC $V_{50}$ (mV) | −38.09 ± 0.93 | −36.01 ± 1.35 | 0.49 |
| | HMN P120 | | |
| | WT ($n = 15$, $N = 7$) | $SOD1^{G93A}$ ($n = 24$, $N = 7$) | *P* value |
| PIC absolute (pA) | −274.60 ± 37.32 | −239.80 ± 29.71 | 0.47 |
| PIC density (pA $pF^{-1}$) | −4.59 ± 0.34 | −4.26 ± 0.45 | 0.60 |
| PIC $V_{50}$ (mV) | −37.48 ± 1.19 | −37.74 ± 1.11 | 0.88 |

$N = 5$; $P = 0.85$; endstage OMNs: WT: 284.98 ± 9.19 Hz, $n = 25$, $N = 6$; $SOD1^{G93A}$: 288.29 ± 9.35 Hz, $n = 26$, $N = 4$; $P = 0.80$; data not shown).

After firing at 40 Hz, adult presymptomatic $SOD1^{G93A}$ HMNs displayed about 20% faster mean $Ca^{2+}$ decay kinetics compared to those of age-matched WT controls, while mean maximal amplitudes and mean areas were not different between $SOD1^{G93A}$ and WT at this low frequency (Figs 4*C* and 5; for values see Supplemental Table S2). This finding suggests that presymptomatic $SOD1^{G93A}$ HMNs are more competent in handling the activity-dependent $Ca^{2+}$ load at moderate firing frequencies. Maximal discharge resulted in significantly higher peak $Ca^{2+}$ amplitudes in presymptomatic $SOD1^{G93A}$ HMNs compared to WT and a trend to smaller $\tau$ and area (Figs 4*C* and 5; Supplemental Table S2). This indicates not only that distinct mechanisms of $Ca^{2+}$ handling might be recruited in different firing frequency ranges but also that they might be differentially affected by $SOD1^{G93A}$ expression.

At disease endstage, more dramatic $SOD1^{G93A}$-mediated changes in activity-dependent $Ca^{2+}$ handling were observed without any differences in resting $Ca^{2+}$ (Supplemental Fig. S2). At 40 Hz, significantly increased stimulation-induced peak amplitudes were recorded in endstage HMNs compared to age-matched WT MNs (Figs 4*D* and 5*A*; Supplemental Table S2). In addition, with increasing stimulation frequencies (Fig. 4*D*, right panel), post-stimulation $Ca^{2+}$ clearance significantly slowed and resulted in an about 40% increased mean $\tau$ and area at maximal frequencies in endstage $SOD1^{G93A}$ HMNs compared to age-matched WT MNs (Figs 4*D* and 5; Supplemental Table S2). Moreover, the activity-dependent $Ca^{2+}$ clearance deficit was very pronounced in about 1/3 of the endstage $SOD1^{G93A}$ HMNs ($n = 8/26$), leading to a right-skewed distribution when plotting the occurrence probability of $\tau$ values (Supplemental Fig. S3). When restricting the analysis to this most affected subpopulation of $SOD1^{G93A}$ HMNs an increase of $\tau$ of about 200% was observed. A similar heterogeneity was not seen in presymptomatic $SOD1^{G93A}$ mice.

In contrast and apart from a small but significant increase in the maximal stimulation peak amplitude, endstage $SOD1^{G93A}$ OMNs did not show any differences in activity-dependent $Ca^{2+}$ handling compared to age-matched WT controls (Figs 4*E* and 5; Supplemental Table S2). This comparative dataset between OMNs and HMNs at disease endstage strongly suggests that the observed changes in $Ca^{2+}$ handling are disease related and specific for the vulnerable target neurons in ALS.

## Diminished mitochondrial $Ca^{2+}$ uptake in endstage $SOD1^{G93A}$ HMNs is independent of the mitochondrial membrane potential

As there is evidence for mitochondrial disturbances in ALS (Cozzolino & Carrì, 2011), we next studied the mitochondrial $Ca^{2+}$ uptake to probe for a potential mitochondrial contribution to the observed $Ca^{2+}$ clearance deficit. FCCP is an uncoupler of the mitochondrial membrane potential ($\Psi_m$) that reduces the driving force for mitochondrial $Ca^{2+}$ uptake. We bath applied 200 nM FCCP during $Ca^{2+}$ imaging (Fig. 6*A* and *B*), which was the maximal FCCP concentration that did not lead to conductance changes of the plasma membrane for at least 45 min during recordings in adult HMNs. Based on previous studies (Brennan *et al.* 2006; Tretter & Adam-Vizi, 2007), we assume that 200 nM FCCP completely blocks or at least significantly reduces the driving force for mitochondrial $Ca^{2+}$ uptake both in WT and $SOD1^{G93A}$ HMNs. For WT HMNs at P70 and P120, we observed a significant 2-fold increase of $\tau$ and signal area already after physiological 40 Hz firing compared to control conditions without uncoupling (Fig. 6*C* and *D*; Supplemental Table S3; similar data for $f_{max}$; see frequency dependence in Fig. 6*E*). These data suggest that

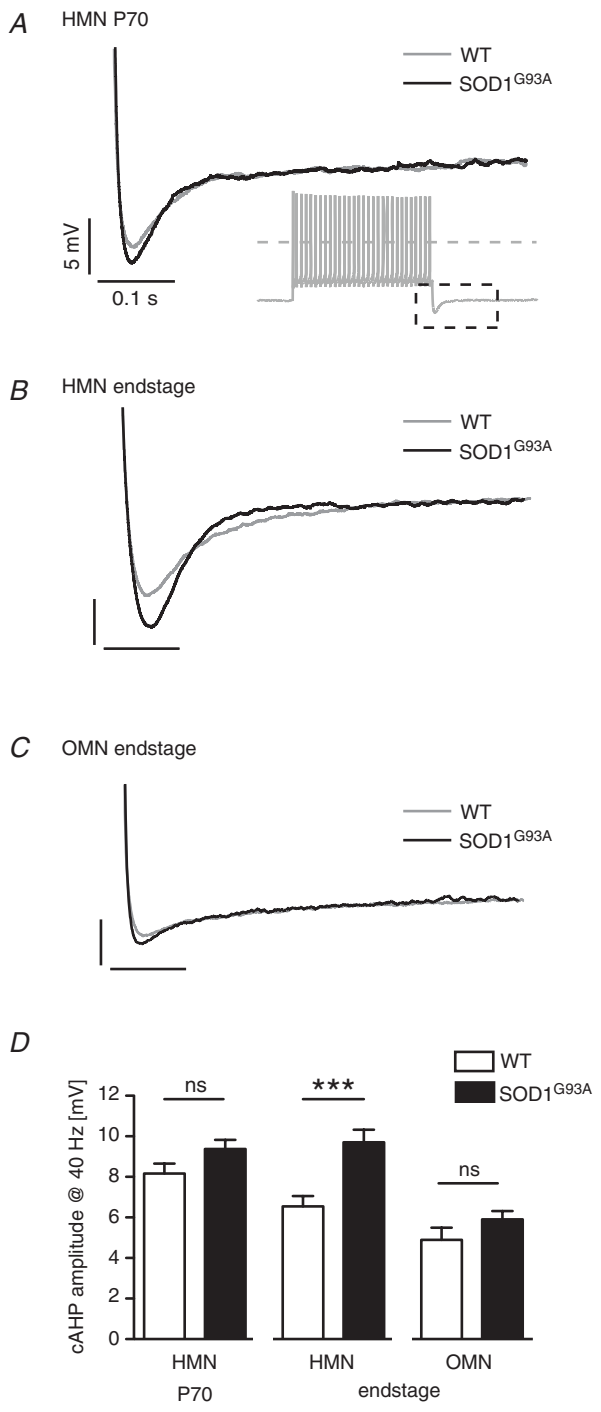


**Figure 3. $Ca^{2+}$-dependent cAHP is increased specifically in endstage vulnerable MNs**
Representative cAHP (compound afterhyperpolarisation in response to a train of action potentials at 40 Hz, see inset; dashed line at 0 mV) of presymptomatic $SOD1^{G93A}$ and age-matched WT HMNs (*A*), endstage $SOD1^{G93A}$ and age-matched WT HMNs (*B*) and endstage $SOD1^{G93A}$ and age-matched WT oculomotor motoneurons (OMNs) (*C*). Note the bigger amplitude of the cAHP in endstage $SOD1^{G93A}$ HMN compared to WT. *D*, mean cAHP amplitudes of WT and $SOD1^{G93A}$ HMNs and OMNs. Statistical significance as indicated ns, not significant. For values see Table 1. Note the significant difference between WT and $SOD1^{G93A}$ specifically in endstage HMNs.

in adult WT HMNs $\Psi_m$-driven mitochondrial $Ca^{2+}$ uptake handles about 50% of the activity-dependent $Ca^{2+}$ load across the entire frequency range.

Presymptomatic P70 $SOD1^{G93A}$ HMNs showed a significantly stronger FCCP-induced impairment of $Ca^{2+}$ clearance than age-matched WT neurons (ANOVA with Tukey's *post hoc* test) with a 3-fold increase in $\tau$ and area compared to control conditions (Fig. 6*C* and *D*; Supplemental Table S3).

In contrast to WT and P70 $SOD1^{G93A}$ neurons, HMNs of endstage $SOD1^{G93A}$ mice did not show any significant change of fura-2 signals in FCCP compared to control conditions neither at 40 Hz nor at $f_{max}$ (Fig. 6*B* and *D*; Supplemental Table S3). These results indicate that $\Psi_m$-driven mitochondrial $Ca^{2+}$ uptake plays at best a minor role in $SOD1^{G93A}$ HMNs at disease endstage and argue for a dramatic remodelling of $Ca^{2+}$ handling during the transition between the adult presymptomatic stage and disease endstage. As we found no evidence for a reduction of the activity-dependent $Ca^{2+}$ load in $SOD1^{G93A}$ HMNs, these results also indicate a compensatory upregulation of $\Psi_m$-independent $Ca^{2+}$ clearance mechanisms in endstage $SOD1^{G93A}$ HMNs. An enhanced $\Psi_m$-independent $Ca^{2+}$ transport in endstage $SOD1^{G93A}$ HMNs enabled fully compensated WT-like $Ca^{2+}$ clearance kinetics at moderate firing frequencies of 40 Hz but increasingly failed in the higher frequency range in 1/3 of the cells (Figs 4 and 5). Consequently, we did not observe any difference in signal area at maximal firing frequency between WT and endstage $SOD1^{G93A}$ in FCCP (representative example in Fig. 6*F*).

The loss of FCCP-sensitive $Ca^{2+}$ transport was selective for vulnerable HMNs and was not observed in resistant $SOD1^{G93A}$ OMNs during disease endstage, which already showed a significant increase of $\tau$ in 80 nM FCCP (maximal tolerable concentration for OMNs; Supplemental Fig. S4, Supplemental Table S3).

## $Ca^{2+}$ clearance deficit is partially compensated by increased plasma membrane $Ca^{2+}$ transport

Next, we aimed to define the upregulated $\Psi_m$-independent $Ca^{2+}$ transport in endstage $SOD1^{G93A}$ HMNs that compensates for the reduced mitochondrial calcium uptake. The two main candidates are $Ca^{2+}$ extrusion across the plasma membrane or sarco-endoplasmic reticulum $Ca^{2+}$ ATPase (SERCA)-mediated uptake into intracellular endoplasmic reticulum (ER) $Ca^{2+}$ storage pools. Given the selective inhibition of SERCA by thapsigargin, we reasoned that coapplication of 200 nM FCCP and 1 $\mu$M thapsigargin would pharmacologically isolate the $Ca^{2+}$ extrusion pathway across the plasma membrane via ATPases (plasma membrane $Ca^{2+}$ ATPase, PMCA) and exchangers ($Na^+/Ca^{2+}$ exchanger, NCX). Accordingly, the

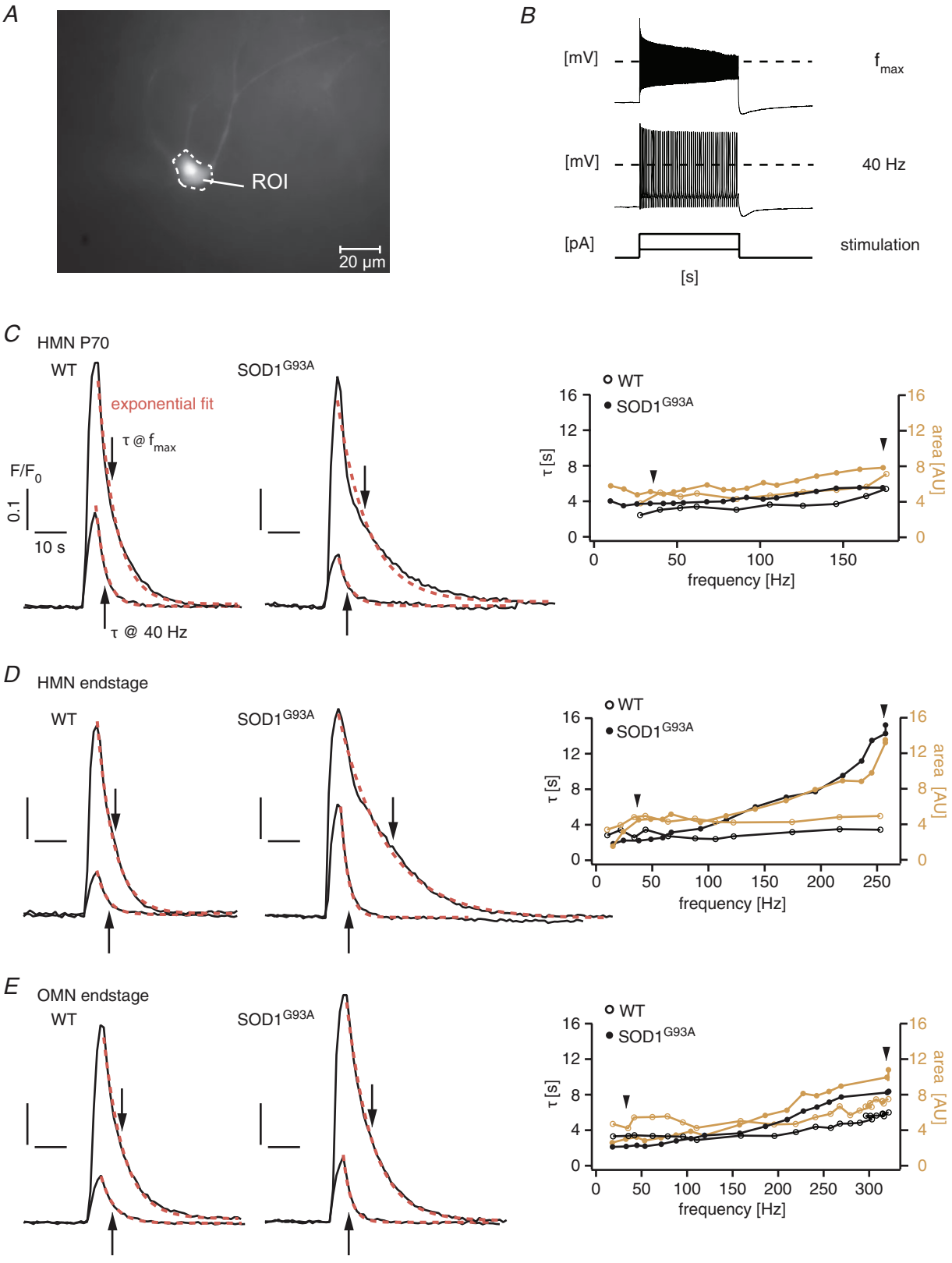


**Figure 4. $Ca^{2+}$ clearance of presymptomatic and endstage HMNs and OMNs**
*A*, HMN loaded with fura-2. The CCD-camera image was taken with excitation wavelength of 357 nm and 1 × 1 binning. $Ca^{2+}$ signals were recorded over the cell soma as a region of interest (ROI). *B*, stimulation protocol for fura-2 $Ca^{2+}$ imaging experiments. Increasing current steps (2 s) evoked repetitive firing. $Ca^{2+}$ signals following

decay kinetics of the fura-2 signal were well described with a single exponential function in the presence of FCCP and thapsigargin (Fig. 7*A*). This combination of specific blockers revealed a frequency-independent difference in the $Ca^{2+}$ clearance kinetics in both WT and endstage $SOD1^{G93A}$ HMNs compared to control conditions ($\tau$ at 40 Hz: WT: $10.54 \pm 1.05$ s, $n = 23$, $N = 5$; $P < 0.001$; $SOD1^{G93A}$: $7.93 \pm 0.83$ s, $n = 22$, $N = 3$; $P < 0.001$; area at 40 Hz: WT: $10.71 \pm 0.92$, $n = 23$, $N = 5$; $P < 0.001$; $SOD1^{G93A}$: $8.83 \pm 0.71$, $n = 22$, $N = 3$; $P < 0.001$; Fig. 7; $f_{max}$ data similar (not shown)). Importantly, the FCCP- and thapsigargin-insensitive $Ca^{2+}$ clearance was significantly faster in endstage $SOD1^{G93A}$ HMNs compared to age-matched controls (ANOVA with Tukey's *post hoc* test). These data suggest that the upregulated $\Psi_m$-independent $Ca^{2+}$ transport was most likely mediated by enhanced $Ca^{2+}$ extrusion across the plasma membrane in endstage $SOD1^{G93A}$ HMNs. Another consequence of this combined thapsigargin-FCCP experiment is that the $Ca^{2+}$ extrusion across the plasma membrane might be fuelled solely by glycolytically produced ATP that would further stimulate plasma membrane transporters and reduce mitochondrial $Ca^{2+}$ uptake.

An inhibition of the ER $Ca^{2+}$ uptake via application of 1 $\mu$M thapsigargin alone (Supplemental Fig. S5) resulted in complex genotype- and frequency-dependent changes in the $Ca^{2+}$ clearance kinetics with no significant difference at 40 Hz in both genotypes compared to the control condition ($\tau$ at 40 Hz: WT: $2.96 \pm 0.22$ s, $n = 23$, $N = 3$, $P = 0.66$; $SOD1^{G93A}$: $3.53 \pm 0.27$ s, $n = 25$, $N = 4$, $P = 0.11$; area at 40 Hz: WT: $4.13 \pm 0.42$, $P = 0.99$; $SOD1^{G93A}$: $4.37 \pm 0.31$, $P = 0.39$). At $f_{max}$, WT HMNs showed slower $Ca^{2+}$ clearance kinetics, whereas endstage $SOD1^{G93A}$ HMN kinetics were faster ($\tau$ at $f_{max}$: WT: $11.15 \pm 1.15$, $P = 0.015$; $SOD1^{G93A}$: $8.31 \pm 0.60$, $P = 0.048$; area at $f_{max}$: WT: $8.82 \pm 0.83$, $P = 0.013$; $SOD1^{G93A}$: $12.74 \pm 1.69$, $P = 0.40$).

## Reduced mitochondrial $Ca^{2+}$ uptake is due to a reduction of mCU transport capacity without changes in mitochondrial membrane potential

Consequently, we carried out experiments to identify the underlying mechanisms of absent $\Psi_m$-dependent $Ca^{2+}$ clearance in $SOD1^{G93A}$ HMNs. As the efficacy of mitochondrial $Ca^{2+}$ buffering depends on both the driving force mainly set by the membrane potential of the inner mitochondrial membrane and the transport capacity, e.g. the number and functional state of mitochondrial $Ca^{2+}$ transporters, we investigated these components separately (Fig. 8).

We used Rh-123 imaging to estimate $\Psi_m$. Figure 8*A* shows Rh-123 fluorescence signals of a representative WT and endstage $SOD1^{G93A}$ HMN under control conditions and in response to maximal $\Psi_m$- uncoupling by acute application of a high concentration of FCCP (5 $\mu$M). Given the similarity of Rh-123 fluorescence changes in response to FCCP in endstage $SOD1^{G93A}$ HMNs and age-matched WT controls ($F/F_0$: WT: $0.092 \pm 0.009$, $n = 22$, $N = 7$; $SOD1^{G93A}$: $0.092 \pm 0.006$, $n = 24$, $N = 8$; $P = 0.98$), we found no evidence for a reduced mitochondrial membrane potential in vulnerable MNs in endstage.

The mitochondrial $Na^+/Ca^{2+}$ exchanger (mNCX) has an important role in the inner mitochondrial membrane mainly for transporting $Ca^{2+}$ out of the mitochondria (Malli & Graier, 2010). By applying 15 $\mu$M CGP37157 via the patch pipette we selectively blocked mNCX in WT and endstage $SOD1^{G93A}$ HMNs (Fig. 8*B*). With CGP37157 the signal decay at maximal firing frequency changed from mono-exponential in control conditions to double-exponential suggesting a reverse mode of operation of the mNCX in our control conditions with $Ca^{2+}$ transported into the mitochondria in exchange with $Na^+$, independent of the genotype. However, we did not observe any significant differences in the fura-2 signal area compared to control conditions in both genotypes (WT: $9.71 \pm 0.88$, $n = 24$, $N = 4$; $SOD1^{G93A}$: $12.33 \pm 0.88$, $n = 25$, $N = 4$; $P = 0.83$). In summary, we found no significant evidence for altered mNCX activity in disease endstage $SOD1^{G93A}$ HMNs.

With no clear evidence for an altered driving force for mitochondrial $Ca^{2+}$ uptake as well as for mNCX function, a plausible alternative explanation might be a reduced $Ca^{2+}$ transport capacity of the mitochondrial $Ca^{2+}$ uniporter (mCU). We used Ru360 as a specific blocker of mCU to probe for its contribution to $Ca^{2+}$ clearance during our stimulation protocols (Fig. 8*C*). After dialysing 20 $\mu$M Ru360 via the patch pipette and stimulating the MNs with increasing current steps, we observed no significant changes of $Ca^{2+}$ clearance kinetics in endstage $SOD1^{G93A}$ HMNs or age-matched controls at

40 Hz and maximal frequency firing ($f_{max}$) were analysed. Dashed lines at 0 mV. *C–E*, ratiometric fura-2 $Ca^{2+}$ signal after 40 Hz or $f_{max}$ for representative age-matched WT (left panel) and $SOD1^{G93A}$ (middle panel) mice of P70 HMN (*C*), endstage HMN (*D*), endstage OMN (*E*). Signal decay was mono-exponentially fitted (red dashed line) to determine time constant $\tau$ (indicated by arrows). Note the slower decay in endstage $SOD1^{G93A}$ at $f_{max}$. Right panel: $\tau$ and normalised signal area (in arbitrary units, AU) plotted against firing frequency of representative WT and $SOD1^{G93A}$ MNs. Note the prominent increase of $\tau$ and area with increasing frequency specifically in endstage $SOD1^{G93A}$ HMNs. Arrowheads indicate the values statistically compared between all cells at 40 Hz and $f_{max}$.

40 Hz firing frequencies (data not shown, Fig. 8*C* upper right panel shows representative frequency dependence), indicating that this low-affinity $Ca^{2+}$ transporter (Malli & Graier, 2010) was not operative at low firing frequencies. In contrast, Ru360 induced complex changes in the post-stimulation time course of the fura-2 signal at maximal firing frequencies. Ru360 treatment led to an initial fura-2 plateau phase up to 12 s duration before the decline phase in endstage $SOD1^{G93A}$ HMNs as well as in age-matched controls. These data suggest that the mCU is not only operative at maximal $Ca^{2+}$ load but also that its inhibition cannot be fully compensated by alternative $Ca^{2+}$ clearance pathways. Quantitatively, $Ca^{2+}$ clearance was significantly impaired by Ru360 in WT but not in endstage $SOD1^{G93A}$ HMNs (area: WT: $16.28 \pm 1.20$, $n = 25, N = 4$; $P < 0.001$; $SOD1^{G93A}$: $16.63 \pm 1.87$, $n = 25$, $N = 5$; $P = 0.10$), indicating a reduced contribution of mCU and/or an enhanced partial compensation by other

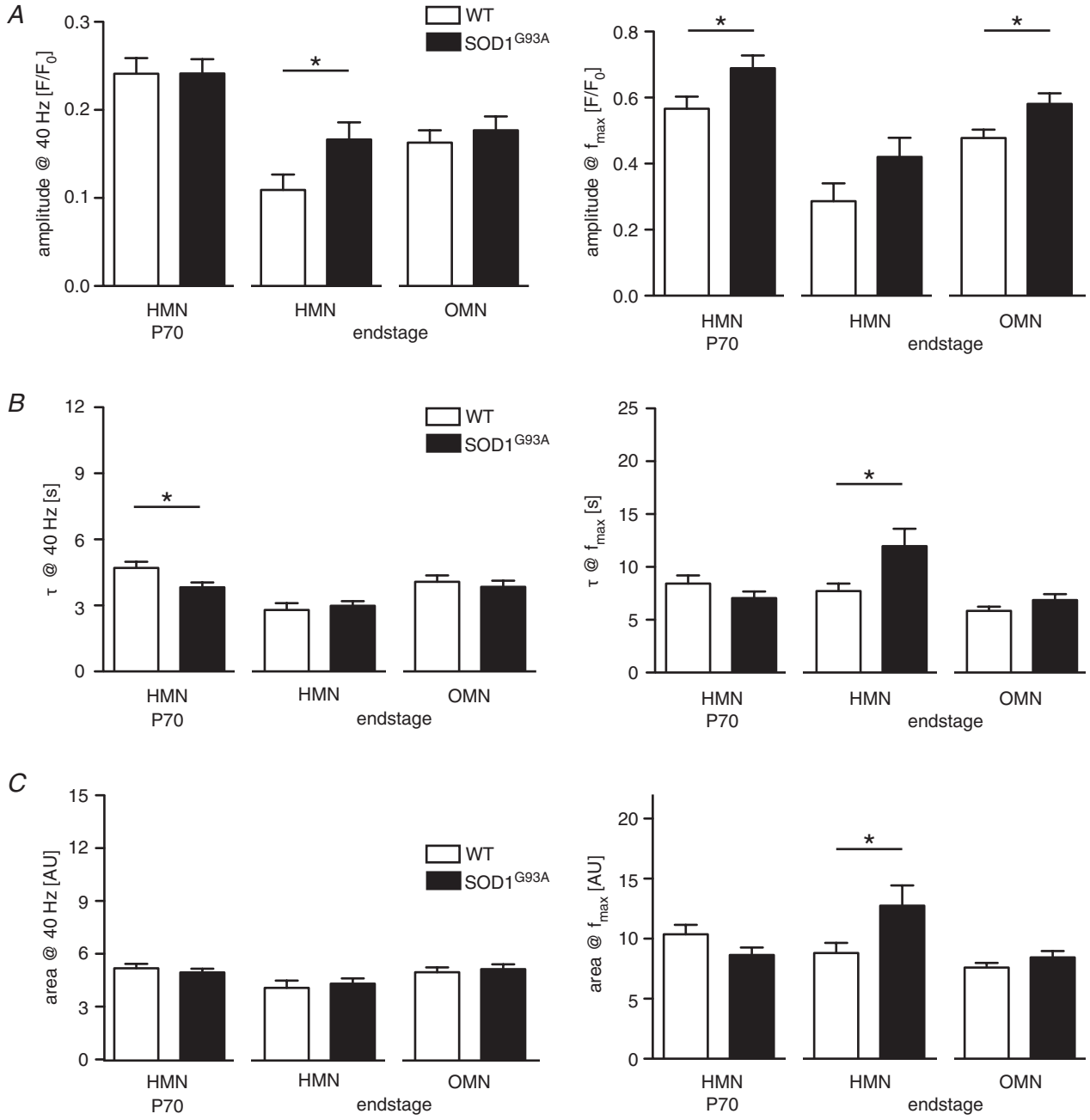


**Figure 5. $Ca^{2+}$ clearance is impaired selectively in vulnerable MNs at disease endstage**
Mean $Ca^{2+}$ signal amplitude (*A*), mean $\tau$ (*B*) and mean signal area (*C*) at 40 Hz (left panels) and $f_{max}$ (right panels). Statistical significance as indicated. For values see Supplemental Table S2. A $Ca^{2+}$ clearance deficit is observed at $f_{max}$ in endstage $SOD1^{G93A}$ HMNs as indicated by significantly larger values for $\tau$ and area.

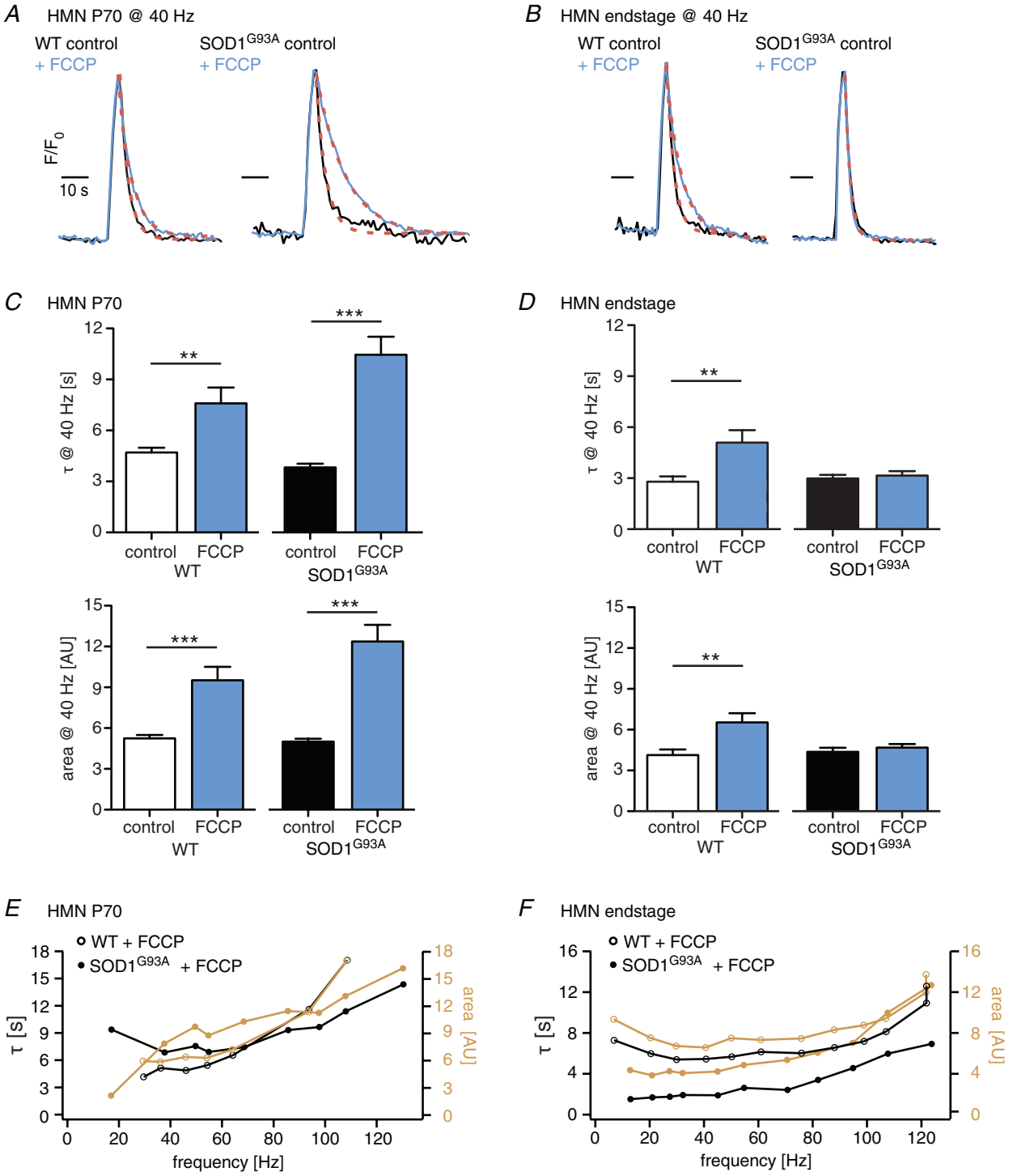


**Figure 6. No change in $Ca^{2+}$ clearance after mitochondrial uncoupling in endstage $SOD1^{G93A}$ HMNs**
*A* and *B*, ratiometric fura-2 $Ca^{2+}$ signal normalised to signal amplitude after 40 Hz firing for representative WT (left panel) and $SOD1^{G93A}$ (right panel) HMNs at P70 (*A*) or disease endstage (*B*) under control conditions (black) and after mitochondrial uncoupling with FCCP (blue). Red dashed lines indicate mono-exponential fit. Note the unaltered kinetics in endstage $SOD1^{G93A}$. *C* and *D*, mean $\tau$ (upper panel) or mean signal area (lower panel) after 40 Hz firing in WT and $SOD1^{G93A}$ HMNs at P70 (*C*) or disease endstage (*D*) under control conditions (same as in Fig. 5) and after FCCP (200 nM) treatment. Statistical significance as indicated. For values see Supplemental Table S3. Note that WT and P70 $SOD1^{G93A}$ HMNs show increased $\tau$ and area in FCCP but endstage $SOD1^{G93A}$ HMNs do not change properties. *E* and *F*, $\tau$ and signal area plotted against firing frequency of WT and $SOD1^{G93A}$ HMNs at P70 (*E*) or disease endstage (*F*) after mitochondrial uncoupling with FCCP.

$Ca^{2+}$ clearance pathways, most likely across the plasma membrane at disease endstage, as we gained evidence for increased plasma membrane $Ca^{2+}$ extrusion in endstage $SOD1^{G93A}$.

To address a possible transcriptional regulation of mCU in $SOD1^{G93A}$ MNs, we quantified cDNA levels of MCU and MICU1, the molecular components of mCU, by combining UV-LMD of pools of 10 individual HMNs from WT and endstage $SOD1^{G93A}$ with RT-qPCR (Fig. 9). Surprisingly, we detected a 70–80% upregulation of cDNA levels in ChAT-positive HMNs from endstage $SOD1^{G93A}$ compared to WT for MICU1 as well as for MCU (MICU1 (normalised expression): WT: $1.00 \pm 0.11$, $n = 21$, $N = 4$; $SOD1^{G93A}$: $1.86 \pm 0.12$, $n = 39$, $N = 4$; $P < 0.001$; MCU: WT: $1.00 \pm 0.14$, $n = 21$, $N = 4$; $SOD1^{G93A}$: $1.68 \pm 0.12$, $n = 39$, $N = 4$; $P < 0.001$). In line with an upregulation of the mRNAs for both subunits, the MCU/MICU1 cDNA ratios of WT HMNs were preserved in $SOD1^{G93A}$ (MCU/MICU1: WT: $1.03 \pm 0.17$, $n = 21$, $N = 4$; $SOD1^{G93A}$: $0.82 \pm 0.06$, $n = 39$, $N = 4$; $P = 0.19$).

In summary, our pharmacological experiments suggest an intact driving force but reduced mCU $Ca^{2+}$ transport efficacy under high-$Ca^{2+}$ loading conditions. These features are present selectively in endstage $SOD1^{G93A}$ HMNs and might cause their activity-dependent, disease-associated $Ca^{2+}$ clearance deficit. The mitochondrial calcium uptake deficit is partially compensated by elevated plasma membrane $Ca^{2+}$ extrusion but the compensation fails in 1/3 of the MNs that survived until disease endstage indicating a mixed population of cells with different disease stages. The

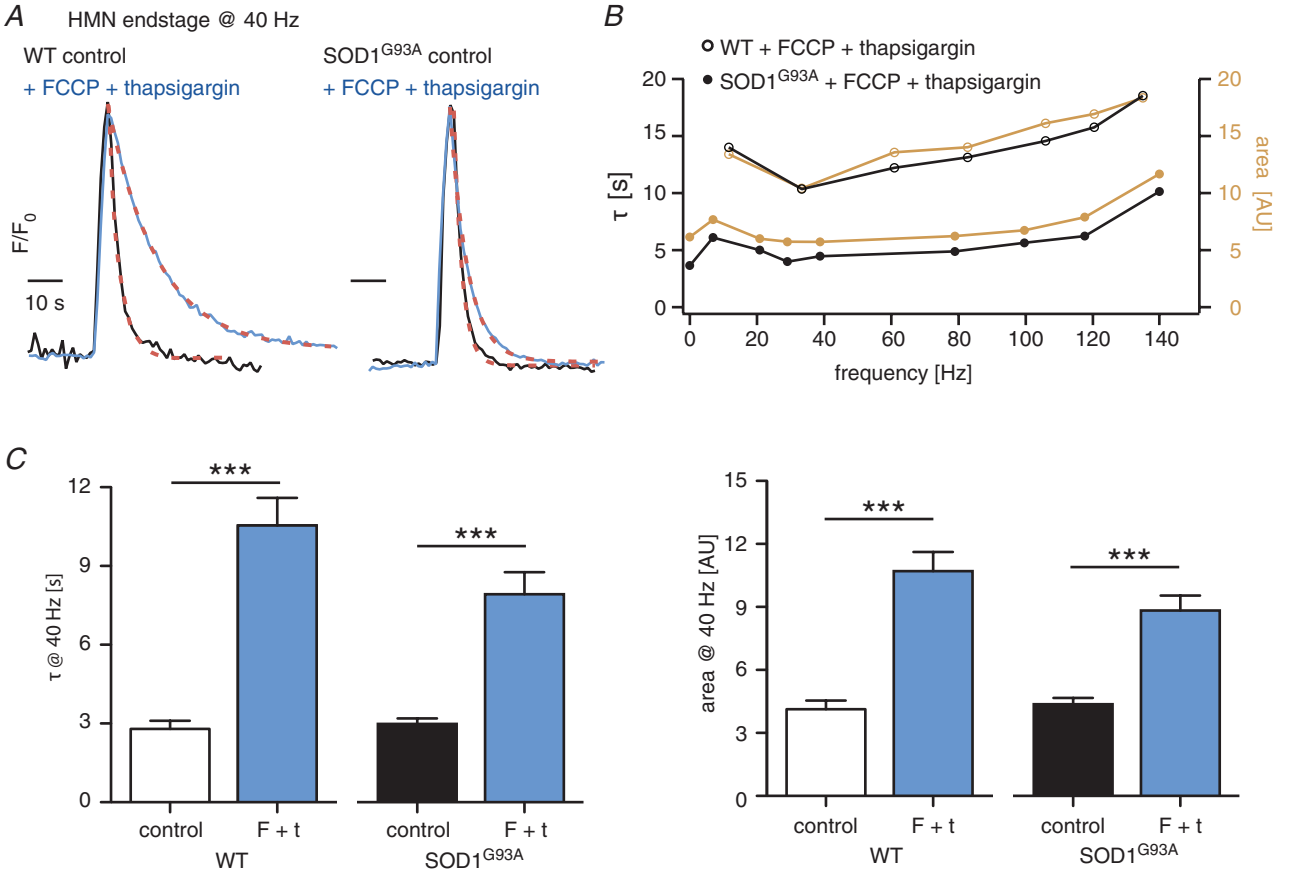


**Figure 7. Plasma membrane $Ca^{2+}$ extrusion is increased in endstage $SOD1^{G93A}$ HMNs**
*A*, ratiometric fura-2 $Ca^{2+}$ signal normalised to the signal amplitude after 40 Hz firing for representative WT (left panel) and endstage $SOD1^{G93A}$ (right panel) HMNs under control conditions (black) and after blocking of mitochondrial and ER $Ca^{2+}$ uptake with FCCP + thapsigargin (blue). Note for WT the slow $Ca^{2+}$ clearance only performed by plasma membrane transporter. *B*, $\tau$ and signal area plotted against firing frequency of a representative WT and endstage $SOD1^{G93A}$ HMN under FCCP + thapsigargin treatment. WT HMNs have larger values for $\tau$ and signal area than endstage $SOD1^{G93A}$ HMNs. *C*, mean $\tau$ (left panel) and area (right panel) at 40 Hz firing of WT and endstage $SOD1^{G93A}$ HMNs under control conditions (same as in Fig. 5) and under FCCP + thapsigargin treatment (F + t). Statistical significance as indicated. For values see text. Note that endstage $SOD1^{G93A}$ HMNs are less affected by blocking of both mitochondrial and ER $Ca^{2+}$ uptake than WT controls, indicating a bigger transport capacity of $Ca^{2+}$ across the plasma membrane.

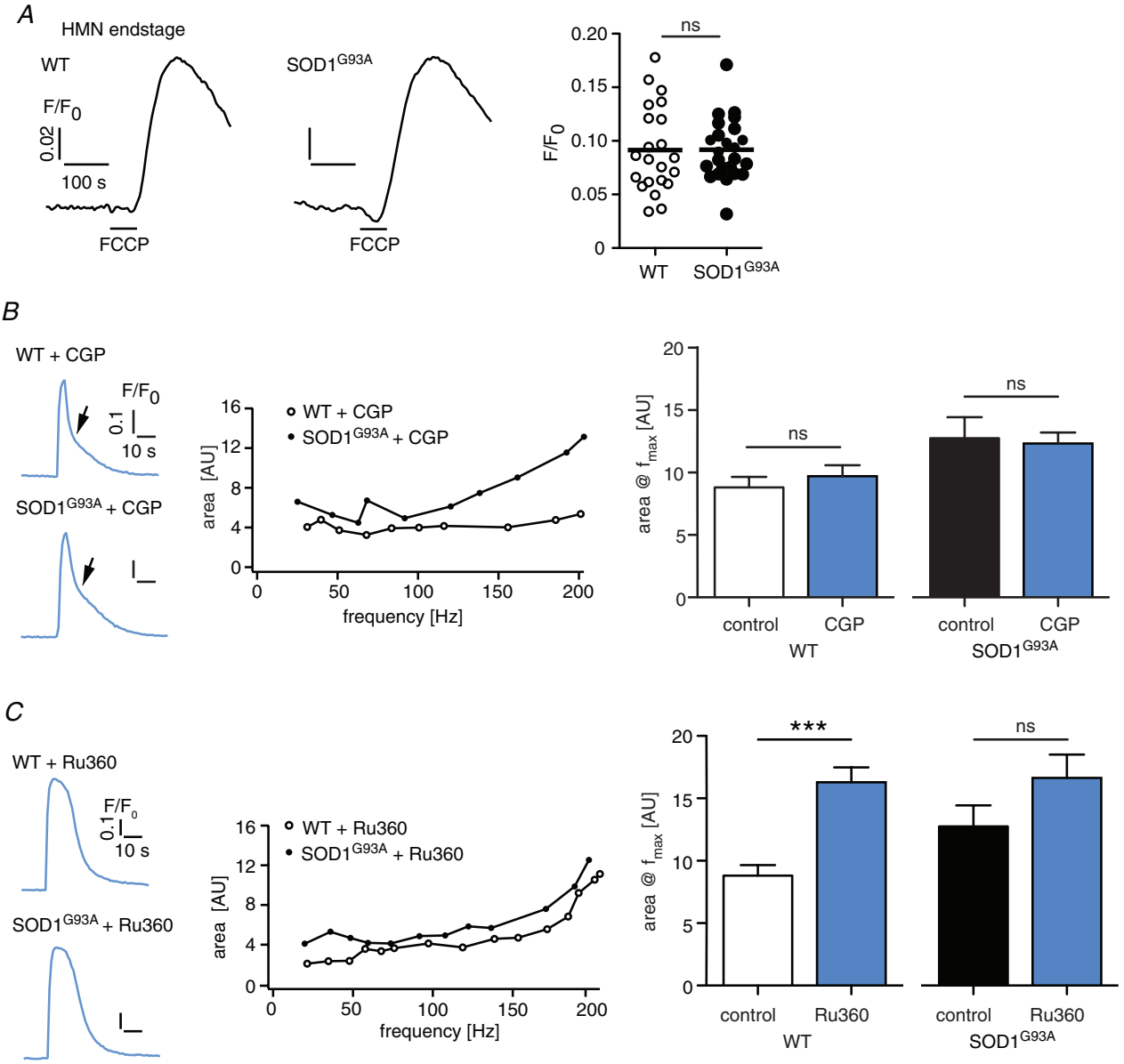


**Figure 8. Similar mitochondrial membrane potential but reduced mCU-dependent transport capacity in endstage SOD1$^{G93A}$ HMNs**

*A*, left panel: Rh-123 fluorescence signal for representative WT and endstage SOD1$^{G93A}$ HMNs. Rh-123 is released from somatic mitochondria after uncoupling with FCCP. Right panel: single cell values and mean Rh-123 signal amplitude after FCCP treatment. Amplitudes are similar in WT and endstage SOD1$^{G93A}$ HMNs, indicating no difference in mitochondrial membrane potentials. *B*, left panel: ratiometric fura-2 $Ca^{2+}$ signal at $f_{max}$ for representative WT and endstage SOD1$^{G93A}$ HMNs under blockade of the mitochondrial $Na^{+}/Ca^{2+}$ exchanger (mNCX) with CGP31757 (CGP). Note the biphasic decay (arrows) indicating that mNCX is in a reverse mode of operation during control conditions transporting $Ca^{2+}$ into the mitochondria. Middle panel: fura-2 signal area plotted against firing frequency of representative WT and endstage SOD1$^{G93A}$ HMNs under CGP treatment. Right panel: mean area at $f_{max}$ of WT and endstage SOD1$^{G93A}$ HMNs under control conditions (same as in Fig. 5) and under CGP treatment. For values see text. mNCX block did not significantly change the fura-2 signal area compared to control conditions independent of the genotype. *C*, left panel: ratiometric fura-2 $Ca^{2+}$ signal at $f_{max}$ for representative WT and endstage SOD1$^{G93A}$ HMNs in Ru360 blocking mCU. Note the signal plateau at maximal $Ca^{2+}$ load. Middle panel: fura-2 signal area plotted against firing frequency of representative WT and endstage SOD1$^{G93A}$ HMNs under Ru360 treatment. WT and SOD1$^{G93A}$ show similar dynamics. Right panel: mean area at $f_{max}$ of WT and endstage SOD1$^{G93A}$ HMNs under control conditions (same as in Fig. 5) and in Ru360. Statistical significance as indicated. ns, not significant. Note that only WT HMNs show significantly increased area in Ru360 compared to control conditions. The difference between WT and SOD1$^{G93A}$ in control conditions is equalised under Ru360 treatment indicating a reduced mCU transport efficacy in endstage SOD1$^{G93A}$ HMNs.

increased gene expression of mCU subunits goes in line with the suggested compensatory endeavour and hints to a more complex, post-transcriptional mechanism of disturbed $Ca^{2+}$ handling.

## Discussion

The mutant SOD1 mouse models stay the best to study the pathogenesis of ALS, although the question remains how representative this model is for human sporadic and familial ALS (Van Den Bosch, 2011). The functional analysis of single MNs including their electrophysiological and $Ca^{2+}$ handling properties in ALS mouse models have been so far largely restricted to cell culture models or early postnatal stages, long before the first clinical symptoms become apparent. Thus, we extended the analysis to provide pathophysiological insights into the adult and clinically most relevant stages, where degeneration mechanisms are probably similar in familial and sporadic ALS and so possibly better referable to human patients. We developed an improved brainstem slice preparation that enabled visually guided patch-clamp recordings in combination with single cell $Ca^{2+}$ imaging of both vulnerable HMNs as well as resistant OMNs throughout the complete life span of the

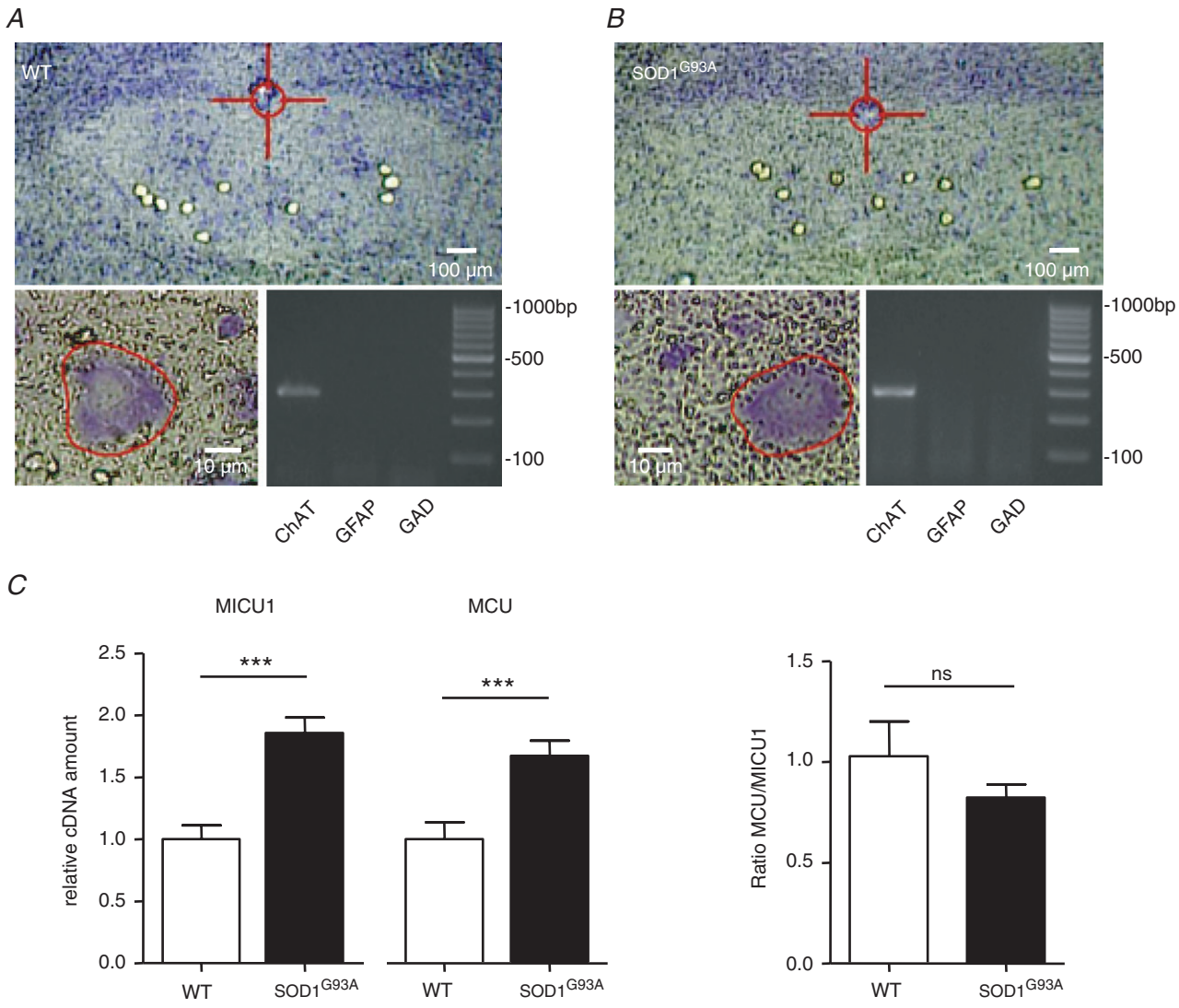


**Figure 9. Elevated mRNA-expression of mCU components in endstage SOD1$^{G93A}$ HMNs**
*A* and *B*, representative coronal brainstem sections before (lower left panel) and after (upper panel) UV-LMD of WT (*A*) and endstage SOD1$^{G93A}$ (*B*) HMNs. Lower right panel: image of agarose gels with multiplex-nested RT-PCR product; note that only ChAT-positive and GAD-negative MN pools were further analysed. *C*, relative cDNA levels for MICU1 and MCU, as well as mean MCU/MICU1 ratios. Note the significantly increased MICU1 and MCU cDNA levels from endstage SOD1$^{G93A}$ HMNs compared to WT. ns, not significant.

SOD1$^{G93A}$ ALS mouse. This preparation allowed for the first time a detailed description of electrophysiological and $Ca^{2+}$ handling properties of single adult brainstem MNs in health and during disease progression. We also established brainstem preparations that allowed UV-LMD and subsequent RT-qPCR of pools of individual, molecularly identified MNs from WT and endstage SOD1$^{G93A}$ ALS mice. In essence, our study identified two pathophysiological states selective for vulnerable MNs in the SOD1$^{G93A}$ ALS mouse: an initial, potentially adaptive hyperexcitable state in adult presymptomatic MNs with an enhanced $Ca^{2+}$ clearance, and a final disease state, which was characterised by normalised excitability and manifest mitochondria-dependent $Ca^{2+}$ clearance deficits. However, our data set does not fully resolve whether individual MNs sequentially express these two phenotypes or represent two different MN populations with distinctly timed pathophysiological manifestations.

### Transient intrinsic hyperexcitability in adult presymptomatic SOD1$^{G93A}$ HMNs

Already in WT animals, electrophysiological properties of MNs change significantly during development in a functionally relevant manner, e.g. 2- to 3-week-old MNs display shorter AP durations, increased cAHP amplitudes or decreased input resistances in comparison to P0–5 MNs (Viana *et al.* 1994; Tsuzuki *et al.* 1995; Berger *et al.* 1996; Carrascal *et al.* 2006; Quinlan *et al.* 2011). For mouse HMNs, patch-clamp data have been reported up to P10 (van Zundert *et al.* 2008), but a recent *in vitro* description (Mitra & Brownstone, 2011) and *in vivo* intracellular recordings of adult spinal MNs (Manuel *et al.* 2009; Meehan *et al.* 2010*b*) suggested ongoing developmental changes of membrane properties after this early juvenile age. Thus, as expected from the general developmental dynamics, our electrophysiological dataset of adult WT HMNs (>P70) differed for some parameters from the published juvenile data (van Zundert *et al.* 2008). Most prominently, adult HMNs possessed an about 4-fold shorter AP followed by a smaller fast AHP. In addition, they also displayed a 2-fold smaller *f–I* slope. Importantly in the context of this study, these properties continued to change in the adult stage, between the ages of P70 and P120. Therefore, properly age-matched WT controls were essential to identify genotype-specific changes in the SOD1$^{G93A}$ mouse. Potential effects of SOD1 overexpression *per se* independent of the G93A mutation were not studied and might be addressed in future studies by using transgenic mice overexpressing wild-type SOD1.

Previous electrophysiological studies on embryonic or juvenile MNs in ALS mouse models identified SOD1$^{G93A}$ genotype-specific intrinsic hyperexcitability and increased persistent inward currents (PICs) (Quinlan, 2011), which were proposed as candidate mechanisms for neurodegeneration. Muscle fasciculations resulting from somatic and axonal hyperexcitability are a well established finding in ALS patients (Mogyoros *et al.* 1998; Kanai *et al.* 2006; Vucic & Kiernan, 2006*a*). In addition, recent *in vivo* intracellular recordings of presymptomatic lumbar MNs in the SOD1$^{G127X}$ mouse (Meehan *et al.* 2010*a*) also support the notion of a hyperexcitability phenotype in ALS. In line with these studies and in particular with a previous one on juvenile (P4–P10) HMNs in the SOD1$^{G93A}$ mice (van Zundert *et al.* 2008), we also found intrinsic hyperexcitability in adult presymptomatic HMNs (P70). However, there was no evidence for increased PICs in SOD1$^{G93A}$ HMNs compared to age-matched WT MNs at this stage. Importantly, we did not detect any signs of hyperexcitability or enhanced $Na^{+}$ PICs in the remaining SOD1$^{G93A}$ HMN population during disease endstage (>P120) compared to age-matched controls. This is in accordance with an axonal excitability study that observed no increased PICs in axons of endstage SOD1$^{G93A}$ mice (Boërio *et al.* 2010). Our results could indicate that hyperexcitability is only a transient phenotype during disease progression in this transgenic ALS model. Consequently, the temporal dissociation of a presymptomatic hyperexcitable stage and the phase of neurodegeneration itself render a direct causal role of intrinsic hyperexcitability for neuronal death less likely. Instead, we favour the idea that hyperexcitability in association with remodelling of $Ca^{2+}$ handling (see below) represents an earlier adaptive (or mal-adaptive) state of vulnerable MNs challenged in ALS, which might be, for example, a developmental phenotype (discussed in Amendola *et al.* 2007; Quinlan *et al.* 2011) or a homeostatic response to extrinsic glutamatergic overexcitation (Van Den Bosch *et al.* 2006) or depolarising GABA action (Fuchs *et al.* 2010). In addition, early energetic deficits (<P60) (Browne *et al.* 2006), hyperexcitability (Vucic & Kiernan, 2006*b*; Pieri *et al.* 2009) and degeneration (<P30) (Ozdinler *et al.* 2011) of cortical upper MNs in the SOD1$^{G93A}$ mouse might be stressors to the lower MNs. In contrast to the SOD1$^{G93A}$ ALS mouse with their fast and synchronised disease progression, adaptive hyperexcitable and non-hyperexcitable endstage MNs might overlap or even coexist throughout a more variable and asynchronous disease progression in individual ALS patients (Ravits & La Spada, 2009).

Our data are not sufficient to decide whether individual MNs indeed progress from the hyperexcitable state to endstage characterised by reduced $Ca^{2+}$ handling capacity. Hyperexcitable MNs might already be degenerated at the analysed late disease stage and the recorded cells at endstage might be those that are more resistant to degeneration. However, at the defined endstage of P120–P130, 28–42% of SOD1$^{G93A}$ HMNs are lost in comparison to >65% in spinal cord (Haenggeli & Kato, 2002; Ferrucci *et al.* 2010; Ringer *et al.* 2012). HMNs

from P120 mice might be in an earlier pathological stage in comparison to spinal cord MNs from animals at the same age. Therefore, it is highly unlikely that we only analysed degeneration-resistant HMNs. However, we cannot exclude that hyperexcitable MNs are present at endstage *in vivo* but are preferentially lost during brain slice preparation for patch-clamp/$Ca^{2+}$ imaging experiments.

## Activity-dependent $Ca^{2+}$ clearance deficit in endstage $SOD1^{G93A}$ HMNs

Apart from defining the transient nature of intrinsic hyperexcitability in the subpopulation of adult $SOD1^{G93A}$ HMNs present in the *in vitro* preparation, the major finding of our study is the identification of a novel endstage-specific phenotype in these neurons. Only in endstage and selective for the vulnerable HMNs compared to resistant OMNs, we detected an activity-dependent deficit of the cytosolic $Ca^{2+}$ clearance. Although altered MN $Ca^{2+}$ handling and buffering have been at the focus of pathophysiological ALS models and theories of differential vulnerability between MN populations for quite some time (Lewinski & Keller, 2005; Grosskreutz *et al.* 2010), our dataset is the first to identify altered $Ca^{2+}$ handling as a cell-type- and disease-stage-selective feature in an ALS model.

We focused our analysis of $Ca^{2+}$ clearance dynamics elicited by 40 Hz and maximal firing in HMNs to study both an intermediate physiological frequency that occurs during respiration-related *in vivo* bursting (Rice *et al.* 2011) and a maximal $Ca^{2+}$ load to probe for the reserve capacity of $Ca^{2+}$ handling in these neurons. Already at 40 Hz, endstage $SOD1^{G93A}$ HMNs showed increased cAHP amplitude. As the cAHP is mainly mediated by SK channels in MNs (Lape & Nistri, 2000), its enhanced amplitude most likely reflects an increase in the global $Ca^{2+}$ concentration, not local $Ca^{2+}$ domains (Fakler & Adelman, 2008), which would have predicted changes also in single AP-induced fast AHPs that are mainly driven by A-type and BK potassium conductances (Storm, 1989; Viana *et al.* 1993). As a consequence, even during physiologically repeated intermediate activity of HMNs, e.g. during respiration, HMNs might suffer from activity-dependent $Ca^{2+}$ overload at disease endstage. *In vivo* $Ca^{2+}$ imaging experiments at endstage are necessary in order to directly test this hypothesis.

Maximal firing *in vitro* unmasked a significant slowing of $Ca^{2+}$ clearance indicative of a dramatically reduced reserve capacity of endstage $SOD1^{G93A}$ HMNs, which is the first direct experimental evidence that altered $Ca^{2+}$ homeostasis is present during the most active period of neurodegeneration in ALS. We expect that activity-dependent $Ca^{2+}$ clearance might also be slowed *in vivo* during disease endstage, where synaptically triggered and intrinsic $Ca^{2+}$ loading are additive resulting from the coincidental opening of $Ca^{2+}$-permeable glutamate receptors (Guatteo *et al.* 2007) and voltage-gated $Ca^{2+}$ channels. Notably, the slower $Ca^{2+}$ clearance kinetics were only apparent in a subset of endstage $SOD1^{G93A}$ HMNs. As the disease will affect single neurons at different time points during progression (focal start and contiguous spread; Ravits & La Spada, 2009), we suggest that this subpopulation of about 30% of MNs represents an advanced stage in the disease progress. Potential cell loss of this subpopulation by the stress of *in vitro* slice preparation might result in an underestimation of their abundance. In any case, pathophysiological heterogeneity is in accordance to the less severe pathological stage in the hypoglossal nucleus compared to the spinal cord discussed above.

## Impaired mitochondrial $Ca^{2+}$ uptake despite intact mitochondrial membrane potential in endstage $SOD1^{G93A}$ HMNs

As we have shown that the $Ca^{2+}$ clearance kinetics of endstage $SOD1^{G93A}$ HMNs are insensitive to uncoupling of the mitochondrial membrane potential ($\Psi_m$) already at physiological firing range, we identified the reduction of $\Psi_m$-driven mitochondrial $Ca^{2+}$ uptake through mitochondrial $Ca^{2+}$ uniporters as a selective pathophysiological feature in endstage $SOD1^{G93A}$ HMNs. These findings are in line with a previous imaging study of endstage $SOD1^{G93A}$ HMNs showing that less $Ca^{2+}$ is stored in mitochondria (Jaiswal & Keller, 2009). However, we found no clear evidence for impairment of mitochondria *per se* in endstage $SOD1^{G93A}$ HMNs, as indicated by their WT-like Rh-123 fluorescence responses to FCCP. Further independent support for functional mitochondria was evident from WT-like fura-2 $Ca^{2+}$ kinetics in response to selective blockers of the mitochondrial $Na^+/Ca^{2+}$ exchanger. Both experiments indicated – at least for the monitored mitochondria localised in the somata of HMNs – that even at endstage they are not significantly depolarised and still possess intact ion transport mechanisms. It is interesting to note that the finding of an intact $\Psi_m$ in $SOD1^{G93A}$ MNs deviates from results presented in earlier reports (Kawamata & Manfredi, 2010; Cozzolino & Carrì, 2011), but the substantial diversity of experimental conditions found for biochemically isolated mitochondria (e.g. Carrì *et al.* 1997), whole-tissue CNS preparations (e.g. Jaiswal & Keller, 2009) and single-cell patch-clamped MNs with pipette-controlled intracellular solutions (this report) might well account for this heterogeneity.

The detected impairment of mitochondrial $Ca^{2+}$ uptake in the presence of an intact mitochondrial membrane potential might be caused by several mechanisms: a transcriptional down-regulation of the genes coding for

transport proteins of mitochondrial $Ca^{2+}$ uptake (e.g. mCU, UCP2/3, Letm1), reduction of the mCU transport efficacy by MICU1 upregulation (Mallilankaraman *et al.* 2012), post-transcriptional deficits in synthesis, maturation and mitochondrial import of the transporter complexes (Li *et al.* 2010) or mislocalisation of mitochondria themselves in relation to $Ca^{2+}$ sources (De Vos *et al.* 2007; Magrané & Manfredi, 2009). Our data do not define which of these potential mechanisms is causal for the reduced mitochondrial calcium uptake in endstage $SOD1^{G93A}$ MNs, but the transcriptional upregulation of mCU subunits might indicate a compensatory mechanism in the remaining MNs.

The contrasting results at 40 Hz showing differences between WT and $SOD1^{G93A}$ with FCCP but not with Ru360 hint to even more complex changes. As the mCU is only recruited at high $Ca^{2+}$ concentrations (Malli & Graier, 2010), more sensitive $Ca^{2+}$ uptake mechanisms like Letm1 (Jiang *et al.* 2009) might also be affected. This could not be directly investigated in this study due to the lack of specific pharmacological agents.

The complex change of $Ca^{2+}$ dynamics after isolated blocking of the ER $Ca^{2+}$ uptake needs to be further investigated. In line with the changes in mitochondrial calcium handling, a mitochondria–ER coupling for normal $Ca^{2+}$ homeostasis (Grosskreutz *et al.* 2010) might be disturbed at disease endstage, leading to the unexpected results of improved calcium clearance with thapsigargin.

### Presymptomatic adaptation and endstage deficit of $Ca^{2+}$ clearance – a mechanistic substrate for differential vulnerability and cell death in ALS?

The faster activity-dependent $Ca^{2+}$ clearance of adult presymptomatic $SOD1^{G93A}$ HMNs together with their larger slowing of clearance kinetics after mitochondrial uncoupling indicated a $SOD1^{G93A}$-associated remodelling of $Ca^{2+}$ clearance compared to WT. The remodelling proceeds from enhanced FCCP-sensitive mitochondrial $Ca^{2+}$ uptake capacity during presymptomatic stages, to a virtual loss of FCCP-sensitive $Ca^{2+}$ clearance and a parallel transcriptional upregulation of mCU subunits as well as an increase of $Ca^{2+}$ extrusion across the plasma membrane shown in endstage $SOD1^{G93A}$ HMNs. These mechanisms might be cell-protective attempts as they were seen in these neurons that survived to a very late disease stage. In line with this theory, increased MICU1 expression was shown to reduce mitochondrial $Ca^{2+}$ uptake and thereby reduces cellular stress (Mallilankaraman *et al.* 2012). However, in 1/3 of the measured endstage MNs the compensation was not sufficient to deal with a high $Ca^{2+}$ load, leading to the observed clearance deficit (for a graphical summary of the suggested changes see Supplemental Fig. S6). Therefore, we suggest this subpopulation to be in an advanced disease stage where compensation fails in the end, leading to cytosolic calcium overload that triggers cell death.

The changes at disease endstage we discovered do not occur in resistant OMNs and might therefore contribute to the differential vulnerability between these two populations. It will be important to study whether spinal MNs in ALS also display these changes in $Ca^{2+}$ handling that we have identified for HMNs. Future studies should address this interpretation by manipulating the activity and expression of mitochondrial (MICU1, MCU, UCP2/3, Letm1) and plasma membrane $Ca^{2+}$ transporters (PMCA, NCX) in vulnerable MNs in a disease-stage-specific manner. Thereby, in the long run, specific neuroprotective intervention targets might be defined for the surprisingly dynamic and selective remodelling of $Ca^{2+}$ handling in MNs vulnerable to ALS.

## References

Alexianu ME, Ho BK, Mohamed AH, La Bella V, Smith RG & Appel SH (1994). The role of calcium-binding proteins in selective motoneuron vulnerability in amyotrophic lateral sclerosis. *Ann Neurol* **36**, 846–858.

Amendola J, Gueritaud JP, d'Incamps BL, Bories C, Liabeuf S, Allene C, Pambo-Pambo A & Durand J (2007). Postnatal electrical and morphological abnormalities in lumbar motoneurons from transgenic mouse models of amyotrophic lateral sclerosis. *Arch Ital Biol* **145**, 311–323.

Berger AJ, Bayliss DA & Viana F (1996). Development of hypoglossal motoneurons. *J Appl Physiol* **81**, 1039–1048.

Boërio D, Kalmar B, Greensmith L & Bostock H (2010). Excitability properties of mouse motor axons in the mutant $SOD1^{G93A}$ model of amyotrophic lateral sclerosis. *Muscle Nerve* **41**, 774–784.

Bories C, Amendola J, Lamotte d'Incamps B & Durand J (2007). Early electrophysiological abnormalities in lumbar motoneurons in a transgenic mouse model of amyotrophic lateral sclerosis. *Eur J Neurosci* **25**, 451–459.

Brennan J, Berry R, Baghai M, Duchen M & Shattock M (2006). FCCP is cardioprotective at concentrations that cause mitochondrial oxidation without detectable depolarisation. *Cardiovasc Res* **72**, 322–330.

Browne SE, Yang L, DiMauro J-P, Fuller SW, Licata SC & Beal MF (2006). Bioenergetic abnormalities in discrete cerebral motor pathways presage spinal cord pathology in the G93A SOD1 mouse model of ALS. *Neurobiol Dis* **22**, 599–610.

Carrascal L, Nieto-Gonzalez JL, Nunez-Abades P & Torres B (2006). Temporal sequence of changes in electrophysiological properties of oculomotor motoneurons during postnatal development. *Neuroscience* **140**, 1223–1237.

Carrì MT, Ferri A, Battistoni A, Famhy L, Gabbianelli R, Poccia F & Rotilio G (1997). Expression of a Cu,Zn superoxide dismutase typical of familial amyotrophic lateral sclerosis induces mitochondrial alteration and increase of cytosolic $Ca^{2+}$ concentration in transfected neuroblastoma SH-SY5Y cells. *FEBS Lett* **414**, 365–368.

Carriedo SG, Yin HZ & Weiss JH (1996). Motor neurons are selectively vulnerable to AMPA/kainate receptor-mediated injury *in vitro*. *J Neurosci* **16**, 4069–4079.

Chiu AY, Zhai P, Dal Canto MC, Peters TM, Kwon YW, Prattis SM & Gurney ME (1995). Age-dependent penetrance of disease in a transgenic mouse model of familial amyotrophic lateral sclerosis. *Mol Cell Neurosci* **6**, 349–362.

Coussee E, De Smet P, Bogaert E, Elens I, Van Damme P, Willems P, Koopman W, Van Den Bosch L & Callewaert G (2011). G37R SOD1 mutant alters mitochondrial complex I activity, $Ca^{2+}$ uptake and ATP production. *Cell Calcium* **49**, 217–225.

Cozzolino M & Carrì MT (2011). Mitochondrial dysfunction in ALS. *Prog Neurobiol* **95**, 133–148.

Damiano M, Starkov AA, Petri S, Kipiani K, Kiaei M, Mattiazzi M, Beal MF & Manfredi G (2006). Neural mitochondrial $Ca^{2+}$ capacity impairment precedes the onset of motor symptoms in G93A Cu/Zn-superoxide dismutase mutant mice. *J Neurochem* **96**, 1349–1361.

De Vos KJ, Chapman AL, Tennant ME, Manser C, Tudor EL, Lau K-F, Brownlees J, Ackerley S, Shaw PJ, McLoughlin DM, Shaw CE, Leigh PN, Miller CCJ & Grierson AJ (2007). Familial amyotrophic lateral sclerosis-linked SOD1 mutants perturb fast axonal transport to reduce axonal mitochondria content. *Hum Mol Genet* **16**, 2720–2728.

Fakler B & Adelman JP (2008). Control of $K_{Ca}$ channels by calcium nano/microdomains. *Neuron* **59**, 873–881.

Ferrucci M, Spalloni A, Bartalucci A, Cantafora E, Fulceri F, Nutini M, Longone P, Paparelli A & Fornai F (2010). A systematic study of brainstem motor nuclei in a mouse model of ALS, the effects of lithium. *Neurobiol Dis* **37**, 370–383.

Fuchs A, Ringer C, Bilkei-Gorzo A, Weihe E, Roeper J & Schütz B (2010). Downregulation of the potassium chloride cotransporter KCC2 in vulnerable motoneurons in the SOD1-G93A mouse model of amyotrophic lateral sclerosis. *J Neuropathol Exp Neurol* **69**, 1057–1070.

Gou-Fabregas M, Garcera A, Mincheva S, Perez-Garcia MJ, Comella JX & Soler RM (2009). Specific vulnerability of mouse spinal cord motoneurons to membrane depolarization. *J Neurochem* **110**, 1842–1854.

Grosskreutz J, Van Den Bosch L & Keller BU (2010). Calcium dysregulation in amyotrophic lateral sclerosis. *Cell Calcium* **47**, 165–174.

Grundemann J, Schlaudraff F, Haeckel O & Liss B (2008). Elevated $\alpha$-synuclein mRNA levels in individual UV-laser-microdissected dopaminergic *substantia nigra* neurons in idiopathic Parkinson's disease. *Nucleic Acids Res* **36**, e38–e38.

Guatteo E, Carunchio I, Pieri M, Albo F, Canu N, Mercuri NB & Zona C (2007). Altered calcium homeostasis in motor neurons following AMPA receptor but not voltage-dependent calcium channels' activation in a genetic model of amyotrophic lateral sclerosis. *Neurobiol Dis* **28**, 90–100.

Gurney ME, Pu H, Chiu AY, Dal Canto MC, Polchow CY, Alexander DD, Caliendo J, Hentati A, Kwon YW & Deng HX (1994). Motor neuron degeneration in mice that express a human Cu,Zn superoxide dismutase mutation. *Science* **264**, 1772–1775.

Haenggeli C & Kato AC (2002). Differential vulnerability of cranial motoneurons in mouse models with motor neuron degeneration. *Neurosci Lett* **335**, 39–43.

Hounsgaard J, Hultborn H, Jespersen B & Kiehn O (1988). Bistability of $\alpha$-motoneurones in the decerebrate cat and in the acute spinal cat after intravenous 5-hydroxytryptophan. *J Physiol* **405**, 345–367.

Jaiswal MK & Keller BU (2009). Cu/Zn superoxide dismutase typical for familial amyotrophic lateral sclerosis increases the vulnerability of mitochondria and perturbs $Ca^{2+}$ homeostasis in $SOD1^{G93A}$ mice. *Mol Pharmacol* **75**, 478–489.

Jiang D, Zhao L & Clapham DE (2009). Genome-wide RNAi screen identifies Letm1 as a mitochondrial $Ca^{2+}/H^{+}$ antiporter. *Science* **326**, 144–147.

Kanai K, Kuwabara S, Misawa S, Tamura N, Ogawara K, Nakata M, Sawai S, Hattori T & Bostock H (2006). Altered axonal excitability properties in amyotrophic lateral sclerosis: impaired potassium channel function related to disease stage. *Brain* **129**, 953–962.

Kawamata H & Manfredi G (2010). Mitochondrial dysfunction and intracellular calcium dysregulation in ALS. *Mech Ageing Dev* **131**, 517–526.

Kiernan MC, Vucic S, Cheah BC, Turner MR, Eisen A, Hardiman O, Burrell JR & Zoing MC (2011). Amyotrophic lateral sclerosis. *Lancet* **377**, 942–955

Kruman II, Pedersen WA, Springer JE & Mattson MP (1999). ALS-linked Cu/Zn-SOD mutation increases vulnerability of motor neurons to excitotoxicity by a mechanism involving increased oxidative stress and perturbed calcium homeostasis. *Exp Neurol* **160**, 28–39.

Kuo JJ, Schonewille M, Siddique T, Schults ANA, Fu R, Bär PR, Anelli R, Heckman CJ & Kroese ABA (2004). Hyperexcitability of cultured spinal motoneurons from presymptomatic ALS mice. *J Neurophysiol* **91**, 571–575.

Kuo JJ, Siddique T, Fu R & Heckman CJ (2005). Increased persistent $Na^{+}$ current and its effect on excitability in motoneurones cultured from mutant SOD1 mice. *J Physiol* **563**, 843–854.

Lape R & Nistri A (2000). Current and voltage clamp studies of the spike medium afterhyperpolarization of hypoglossal motoneurons in a rat brain stem slice preparation. *J Neurophysiol* **83**, 2987–2995.

Lewinski von F, Fuchs J, Vanselow BK & Keller BU (2008). Low $Ca^{2+}$ buffering in hypoglossal motoneurons of mutant $SOD1^{G93A}$ mice. *Neurosci Lett* **445**, 224–228.

Lewinski von F & Keller BU (2005). $Ca^{2+}$, mitochondria and selective motoneuron vulnerability: implications for ALS. *Trends Neurosci* **28**, 494–500.

Li Q, Vande Velde C, Israelson A, Xie J, Bailey AO, Dong M-Q, Chun S-J, Roy T, Winer L, Yates JR, Capaldi RA, Cleveland DW & Miller TM (2010). ALS-linked mutant superoxide dismutase 1 (SOD1) alters mitochondrial protein composition and decreases protein import. *Proc Natl Acad Sci U S A* **107**, 21146–21151.

Magrané J & Manfredi G (2009). Mitochondrial function, morphology, and axonal transport in amyotrophic lateral sclerosis. *Antioxid Redox Signal* **11**, 1615–1626.

Malli R & Graier WF (2010). Mitochondrial $Ca^{2+}$ channels: Great unknowns with important functions. *FEBS Lett* **584**, 1942–1947.

Mallilankaraman K, Doonan P, Cárdenas C, Chandramoorthy HC, Müller M, Miller R, Hoffman NE, Gandhirajan RK, Molgó J, Birnbaum MJ, Rothberg BS, Mak DO, Foskett JK & Madesh M (2012). MICU1 is an essential gatekeeper for MCU-mediated mitochondrial $Ca^{2+}$ uptake that regulates cell survival. *Cell* **151**, 630–644.

Manuel M, Iglesias C, Donnet M, Leroy F, Heckman CJ & Zytnicki D (2009). Fast kinetics, high-frequency oscillations, and subprimary firing range in adult mouse spinal motoneurons. *J Neurosci* **29**, 11246–11256.

Meehan CF, Moldovan M, Marklund SL, Graffmo KS, Nielsen JB & Hultborn H (2010*a*). Intrinsic properties of lumbar motor neurones in the adult G127insTGGG superoxide dismutase-1 mutant mouse *in vivo*: evidence for increased persistent inward currents. *Acta Physiol (Oxf)* **200**, 361–376.

Meehan CF, Sukiasyan N, Zhang M, Nielsen JB & Hultborn H (2010*b*). Intrinsic properties of mouse lumbar motoneurons revealed by intracellular recording *in vivo*. *J Neurophysiol* **103**, 2599–2610.

Mitra P & Brownstone RM (2011). An *in vitro* spinal cord slice preparation for recording from lumbar motoneurons of the adult mouse. *J Neurophysiol* **103**, 728–741.

Mogyoros I, Kiernan MC, Burke D & Bostock H (1998). Strength-duration properties of sensory and motor axons in amyotrophic lateral sclerosis. *Brain* **121**, 851–859.

Nguyen KT, García-Chacón LE, Barrett JN, Barrett EF & David G (2009). The $\Psi_m$ depolarization that accompanies mitochondrial $Ca^{2+}$ uptake is greater in mutant SOD1 than in wild-type mouse motor terminals. *Proc Natl Acad Sci U S A* **106**, 2007–2011.

Nimchinsky EA, Young WG, Yeung G, Shah RA, Gordon JW, Bloom FE, Morrison JH & Hof PR (2000). Differential vulnerability of oculomotor, facial, and hypoglossal nuclei in G86R superoxide dismutase transgenic mice. *J Comp Neurol* **416**, 112–125.

Ozdinler PH, Benn S, Yamamoto TH, Güzel M, Brown RH & Macklis JD (2011). Corticospinal motor neurons and related subcerebral projection neurons undergo early and specific neurodegeneration in $hSOD1G^{93}A$ transgenic ALS mice. *J Neurosci* **31**, 4166–4177.

Pambo-Pambo A, Durand J & Gueritaud J-P (2009). Early excitability changes in lumbar motoneurons of transgenic $SOD1^{G85R}$ and $SOD1^{G93A-Low}$ mice. *J Neurophysiol* **102**, 3627–3642.

Pieri M, Albo F, Gaetti C, Spalloni A, Bengtson CP, Longone P, Cavalcanti S & Zona C (2003). Altered excitability of motor neurons in a transgenic mouse model of familial amyotrophic lateral sclerosis. *Neurosci Lett* **351**, 153–156.

Pieri M, Carunchio I, Curcio L, Mercuri NB & Zona C (2009). Increased persistent sodium current determines cortical hyperexcitability in a genetic model of amyotrophic lateral sclerosis. *Exp Neurol* **215**, 368–379.

Quinlan KA (2011). Links between electrophysiological and molecular pathology of amyotrophic lateral sclerosis. *Integr Comp Biol* **51**, 913–925.

Quinlan KA, Schuster JE, Fu R, Siddique T & Heckman CJ (2011). Altered postnatal maturation of electrical properties in spinal motoneurons in a mouse model of amyotrophic lateral sclerosis. *J Physiol* **589**, 2245–2260.

Ravits JM & La Spada AR (2009). ALS motor phenotype heterogeneity, focality, and spread: deconstructing motor neuron degeneration. *Neurology* **73**, 805–811.

Rice AD, Fuglevand AJ, Laine CM & Fregosi RF (2011). Synchronization of presynaptic input to motor units of tongue, inspiratory intercostal and diaphragm muscles. *J Neurophysiol* **105**, 2330–2336.

Ringer C, Weihe E & Schütz B (2012). Calcitonin gene-related peptide expression levels predict motor neuron vulnerability in the superoxide dismutase 1-G93A mouse model of amyotrophic lateral sclerosis. *Neurobiol Dis* **45**, 547–554.

Schütz B (2005). Imbalanced excitatory to inhibitory synaptic input precedes motor neuron degeneration in an animal model of amyotrophic lateral sclerosis. *Neurobiol Dis* **20**, 131–140.

Solomon JA, Tarnopolsky MA & Hamadeh MJ (2011). One universal common endpoint in mouse models of amyotrophic lateral sclerosis. *PLoS ONE* **6**, e20582.

Storm JF (1989). An after-hyperpolarization of medium duration in rat hippocampal pyramidal cells. *J Physiol* **409**, 171–190.

Ticozzi N, Tiloca C, Morelli C, Colombrita C, Poletti B, Doretti A, Maderna L, Messina S, Ratti A & Silani V (2011). Genetics of familial amyotrophic lateral sclerosis. *Arch Ital Biol* **149**, 65–82.

Tretter L & Adam-Vizi V (2007). Uncoupling is without an effect on the production of reactive oxygen species by *in situ* synaptic mitochondria. *J Neurochem* **103**, 1864–1871.

Tsuzuki S, Yoshida S, Yamamoto T & Oka H (1995). Developmental changes in the electrophysiological properties of neonatal rat oculomotor neurons studied *in vitro*. *Neurosci Res* **23**, 389–397.

Van Den Bosch L (2011). Genetic rodent models of amyotrophic lateral sclerosis. *J Biomed Biotechnol* **2011**, 348765.

Van Den Bosch L, Van Damme P, Bogaert E & Robberecht W (2006). The role of excitotoxicity in the pathogenesis of amyotrophic lateral sclerosis. *Biochim Biophys Acta* **1762**, 1068–1082.

Vanselow BK & Keller BU (2000). Calcium dynamics and buffering in oculomotor neurones from mouse that are particularly resistant during amyotrophic lateral sclerosis (ALS)-related motoneurone disease. *J Physiol* **525**, 433–445.

van Zundert B, Peuscher MH, Hynynen M, Chen A, Neve RL, Brown RH, Constantine-Paton M & Bellingham MC (2008). Neonatal neuronal circuitry shows hyperexcitable disturbance in a mouse model of the adult-onset neurodegenerative disease amyotrophic lateral sclerosis. *J Neurosci* **28**, 10864–10874.

Viana F, Bayliss DA & Berger AJ (1993). Multiple potassium conductances and their role in action potential repolarization and repetitive firing behavior of neonatal rat hypoglossal motoneurons. *J Neurophysiol* **69**, 2150–2163.

Viana F, Bayliss DA & Berger AJ (1994). Postnatal changes in rat hypoglossal motoneuron membrane properties. *Neuroscience* **59**, 131–148.

Vila L, Barrett EF & Barrett JN (2003). Stimulation-induced mitochondrial [$Ca^{2+}$] elevations in mouse motor terminals: comparison of wild-type with SOD1-G93A. *J Physiol* **549**, 719–728.

Vucic S & Kiernan MC (2006*a*). Axonal excitability properties in amyotrophic lateral sclerosis. *Clin Neurophysiol* **117**, 1458–1466.

Vucic S & Kiernan MC (2006*b*). Novel threshold tracking techniques suggest that cortical hyperexcitability is an early feature of motor neuron disease. *Brain* **129**, 2436–2446.

Vucic S & Kiernan MC (2010). Upregulation of persistent sodium conductances in familial ALS. *J Neurol Neurosurg Psychiatry* **81**, 222–227.

## Author contributions

The experiments were designed by A.F., B.L., B.U.K. and J.R. Patch-clamp and imaging experiments as well as immunohistochemistry were performed and analysed by A.F. and S.K. in Frankfurt. Laser microdissection and molecular biology were performed and analysed by T.M. and J.D. in Ulm. A.F. wrote the draft manuscript. B.S., B.L., B.U.K. and J.R. supported in interpreting the data and revising the manuscript. All authors approved the final version of the manuscript.

## Acknowledgements

We thank Ole Kiehn, Sabine Krabbe and Julia Schiemann for comments on the manuscript and Jan Gründemann for providing IGOR Pro codes. This work was supported by the MD and PhD programmes for Experimental & Molecular Medicine of Ulm University (T.M., J.D.), SFB 815 (J.R.) and BMBF/EU Program Eranet (project number 01EW0912) Goettingen (A.F.).